Award Number: W81XWH-13-1-0194

TITLE: Optically Based Rapid Screening Method for Proven Optimal Treatment Strategies Before Treatment Begins

PRINCIPAL INVESTIGATOR: Melissa C. Skala, Ph.D.

CONTRACTING ORGANIZATION: Vanderbilt University
Nashville, TN 37235-0002

REPORT DATE: August 2015

TYPE OF REPORT: Annual

PREPARED FOR: U.S. Army Medical Research and Materiel Command
                        Fort Detrick, Maryland 21702-5012

REPORT DOCUMENTATION PAGE

Form Approved
OMB No. 0704-0188

Public reporting burden for this collection of information is estimated to average 1 hour per response, including the time for reviewing instructions, searching existing data sources, gathering and maintaining the data needed, and completing and reviewing this collection of information. Send comments regarding this burden estimate or any other aspect of this collection of information, including suggestions for reducing this burden to Department of Defense, Washington Headquarters Services, Directorate for Information Operations and Reports (0704-0188), 1215 Jefferson Davis Highway, Suite 1204, Arlington, VA 22202-4302. Respondents should be aware that notwithstanding any other provision of law, no person shall be subject to any penalty for failing to comply with a collection of information if it does not display a currently valid OMB control number. **PLEASE DO NOT RETURN YOUR FORM TO THE ABOVE ADDRESS.**

1. REPORT DATE	2. REPORT TYPE	3. DATES COVERED
August 2015	Annual	15 July 2014 – 14 Jul 2015

4. TITLE AND SUBTITLE	5a. CONTRACT NUMBER
Optically Based Rapid Screening Method for Proven Optimal Treatment Strategies Before Treatment Begins	
	5b. GRANT NUMBER W81XWH-13-1-0194
	5c. PROGRAM ELEMENT NUMBER

6. AUTHOR(S)	5d. PROJECT NUMBER
Melissa C. Skala, Ph.D.	
	5e. TASK NUMBER
	5f. WORK UNIT NUMBER
E-Mail: m.skala@vanderbilt.edu	

7. PERFORMING ORGANIZATION NAME(S) AND ADDRESS(ES)	8. PERFORMING ORGANIZATION REPORT NUMBER
Vanderbilt University Nashville, TN 37235-0002	

9. SPONSORING / MONITORING AGENCY NAME(S) AND ADDRESS(ES)	10. SPONSOR/MONITOR'S ACRONYM(S)
U.S. Army Medical Research and Materiel Command Fort Detrick, Maryland 21702-5012	
	11. SPONSOR/MONITOR'S REPORT NUMBER(S)

12. DISTRIBUTION / AVAILABILITY STATEMENT
Approved for Public Release; Distribution Unlimited

13. SUPPLEMENTARY NOTES

14. ABSTRACT

This award seeks to develop high-throughput optical metabolic imaging (OMI) of primary breast tumor organoids (three-dimensional cultures of tumors) to rapidly test/screen breast cancer therapeutics as a strategy to streamline drug development and provide individualized treatment. The results outlined in this progress report indicate that OMI in primary breast tumor organoids can provide early, sensitive measures of treatment response. This system can therefore be used to streamline pre-clinical drug development, by reducing the number of animals, cost, and time required to screen new drugs and drug combinations. The feasibility of OMI measurements in organoids derived from primary human breast tumors has also been demonstrated, with the exciting possibility of providing individualized drug screens in patients before the patient is ever treated. This personalized drug planning approach could reduce toxicities of ineffective treatments, and enable improved outcomes through early, effective interventions. The single-cell analysis capabilities of this technique also have the potential to identify drug combinations that will eliminate treatment-resistant sub-populations of cells that are likely to cause metastases.

15. SUBJECT TERMS
Breast cancer, therapeutic resistance, personalized treatment, novel therapeutics, optical imaging, metabolism

16. SECURITY CLASSIFICATION OF:			17. LIMITATION OF ABSTRACT	18. NUMBER OF PAGES	19a. NAME OF RESPONSIBLE PERSON USAMRMC
a. REPORT U	**b. ABSTRACT** U	**c. THIS PAGE** U	UU	32	**19b. TELEPHONE NUMBER** *(include area code)*

Table of Contents

INTRODUCTION

This award seeks to develop high-throughput optical metabolic imaging (OMI) of primary breast tumor organoids (three-dimensional cultures of tumors) to rapidly test/screen breast cancer therapeutics as a strategy to streamline drug development and provide individualized treatment. This award tests the hypothesis that early changes in tumor cell metabolism as measured by OMI can be used to predict breast tumor response to multiple treatment conditions. The award has three aims. The first is to determine the earliest time point when therapy-induced changes in OMI can be detected. The second is to measure dose-dependent changes in metabolism in response to chemotherapeutic drugs. The third is to compare the results from OMI in patient tissue organoids to actual patient response determined from standard-of-care.

BODY

Aim 1: Determine the earliest time-point at which therapeutically-induced metabolic changes can be measured. (Months 1-24).

     1a.   Regulatory review and approval for animal studies (months 1-2).
Completed.

     1b.   Measure mouse organoid response to drug treatments alone and in combination over a time course with n=480 samples from 9 mice using optical metabolic imaging (**OMI**) (months 3-15).
Completed. The details of this work are described in the previous progress report and in our published paper[1].

     1c.   Measure *in vivo* response to drug treatments alone and in combination over a time course with n=270 mice using OMI (months 3-24).
Completed. The details of this work are described in the previous progress report and in our published paper[1].

     1d.   Analyze OMI data collected from organoid and *in vivo* time-course experiments (months 3-24).
Completed. The details of this work are described in the previous progress report and in our published paper[1].

     1e.   Perform immunohistochemistry (IHC) analysis on organoids (from 1b) and tumors imaged *in vivo* (from 1c) (months 3-24).
Completed. The details of this work are described in the previous progress report and in our published paper[1].

Milestone #1: These experiments will validate our organoid-OMI methods relative to *in vivo* measures and gold standards (IHC) with respect to *temporal* response. These experiments will also guide the selection of time-points for use in future studies.

Aim 2: Measure dose-dependent metabolic changes due to clinically-relevant breast cancer drugs. (Months 13-36).

     2a.   Measure mouse organoid response to drug treatments alone and in combination over a dosage range with n=540 samples from 9 mice using OMI (months 13-24).
This task is currently underway.

     2b.   Measure *in vivo* response to drug treatments alone and in combination over a dosage range with n=200 mice using OMI (months 13-33).
This task is currently underway.

     2c.   Analyze OMI data collected from organoid and *in vivo* dose-response experiments (months 13-36).
This task is currently underway.

2d.   Perform IHC analysis on organoids (from 2a) and tumors imaged *in vivo* (from 2b) (months 13-36).

This task is currently underway.

Milestone #2: This aim will validate our organoid-OMI methods relative to *in vivo* measures and gold standards (IHC) with respect to *dose* response. This work will set the stage for future dose-response studies of breast cancer therapeutics, potentially informing on the optimal drug concentrations for use in patients.
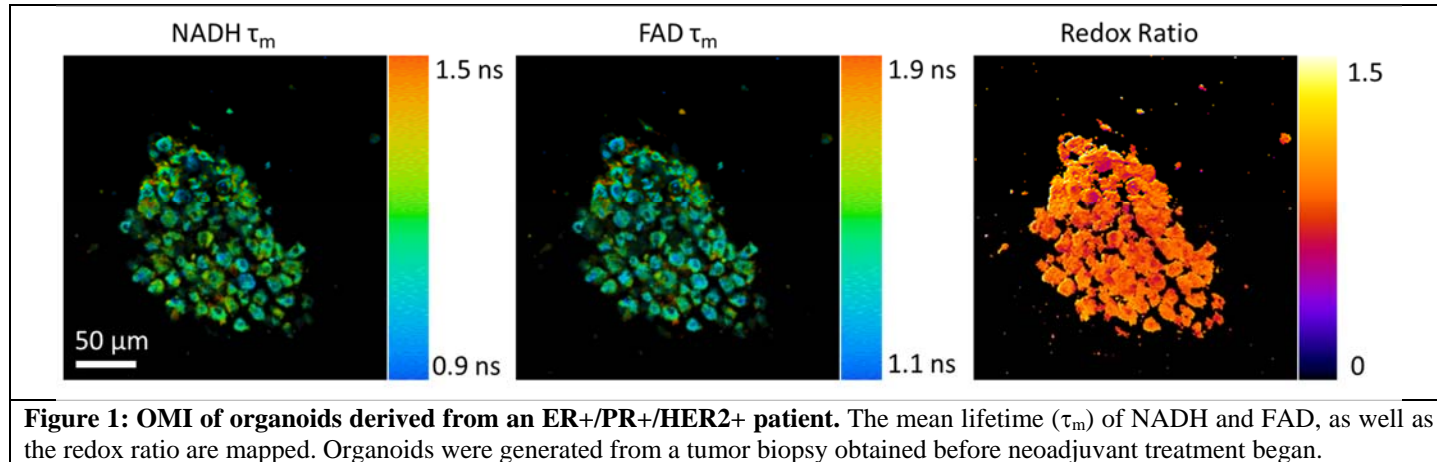
Aim 3: Compare the results of OMI-measured response in human tissue organoids with current clinical measures of response (Months 1-36).

3a.   Regulatory review and approval for human studies (months 1-2).

Completed. IRB# BRE140263 and BRE03103 at Vanderbilt.

3b.   Measure human organoid response to drug treatments alone and in combination from n=50 human breast tumor surgical specimens using OMI (months 3-36). <u>Quarterly enrollment target of 4-5 patients.</u>

This task is currently underway. We have completed measurements in 18 patients so far, 6 of which were reported in our published paper[1]. Representative images from an additional, unpublished patient are included below in Fig. 1.

Figure 1: OMI of organoids derived from an ER+/PR+/HER2+ patient. The mean lifetime (τ_m) of NADH and FAD, as well as the redox ratio are mapped. Organoids were generated from a tumor biopsy obtained before neoadjuvant treatment began.
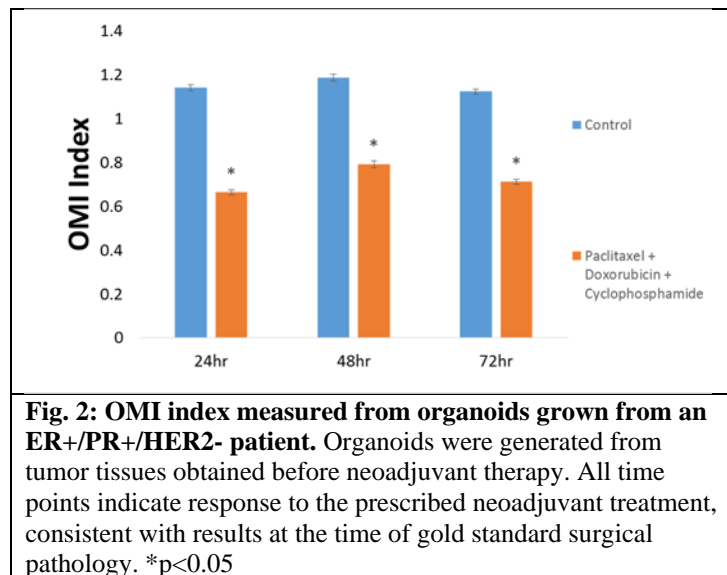
3c.   Collect and analyze surgical pathology and FDG-PET results from patients recruited for this study (months 3-36).

This task is currently underway. For example, the patient shown in Fig. 1 had a 21x10x15mm tumor before neoadjuvant therapy, showed good clinical response to chemotherapy with marked reduction in the size of her tumor both by exam and imaging after 3.5 months of neoadjuvant therapy. Her tumor size reduced to 17x8x12mm, she received a partial mastectomy, and no metastatic lymph nodes found.

3d.   Analyze OMI data collected from human organoid experiments (months 3-36).

This task is currently underway and some data is published [1]. For example, another patient shown in Fig. 2 showed decreases in the OMI index upon treatment with her prescribed neoadjuvant therapy. Consistent with OMI results, she showed significant clinical response to neoadjuvant treatment, and underwent bilateral mastectomy. These OMI results are also consistent with significant FDG uptake in the tumor.

Fig. 2: OMI index measured from organoids grown from an ER+/PR+/HER2- patient. Organoids were generated from tumor tissues obtained before neoadjuvant therapy. All time points indicate response to the prescribed neoadjuvant treatment, consistent with results at the time of gold standard surgical pathology. $*p<0.05$

3e.   Perform IHC analysis on human organoid tissues (months 3-36).
This task is currently underway, and some data is published [1].

Milestone #3: The results from this aim will assess the clinical utility of the organoid-OMI approach, and its accuracy with respect to gold standards (surgical pathology) and standard measures of response (FDG-PET). Ultimately, this work could provide a feasible path for high-throughput assessment of optimal treatment methods for breast cancer patients before treatment begins, significantly reducing morbidity and mortality.

KEY RESEARCH ACCOMPLISHMENTS:
- OMI measurements in organoids can resolve multi-drug response within 24-72 hours of treatment that are in agreement with gold standards of *in vivo* response (tumor volume, IHC).
- It is feasible to grow primary human tumor organoids from fresh breast tumor specimens.
- OMI measurements in primary human tumor organoids agree with standard IHC measures of response.
- OMI can resolve response on a cellular level, in both mouse xenografts and human tumors.
- Preliminary data (Fig. 2) indicate that OMI measures of response to neoadjuvant treatment in patient-derived organoids obtained before neoadjuvant treatment commences is accurate with respect to gold standard surgical pathology after months of neoadjuvant therapy.

REPORTABLE OUTCOMES
Manuscripts:
1. AJ Walsh, RS Cook, CL Arteaga, MC Skala. Optical metabolic imaging of live tissue cultures. SPIE Proceedings. (2013) 8588.
2. AJ Walsh, RS Cook, HC Manning, DJ Hicks, A Lafontant, CL Arteaga, and MC Skala. Optical metabolic imaging identifies breast cancer glycolytic levels, sub-types, and early treatment response. Cancer Research (2013) Oct 15;73(20):6164-74.
3. AJ Walsh, MC Skala. An automated image processing routine for segmentation of cell cytoplasms in high-resolution autofluorescence images. SPIE Proceedings. (2014) 8948.
4. AJ Walsh, RS Cook, ME Sanders, L Aurisicchio, G Ciliberto, CL Arteaga, and MC Skala. Quantitative optical imaging of primary tumor organoid metabolism predicts drug response in breast cancer. Cancer Research (2014) Sep 15;74(18):5184-5194.
5. DR McCormack, AJ Walsh, WW Sit, CL Arteaga, J Chen, RS Cook, and MC Skala. In vivo hyperspectral imaging of microvessel response to trastuzumab treatment in breast cancer xenografts. Biomed. Opt. Express 5, 2247-2261 (2014).

6. TM Cannon, AT Shah, and MC Skala. Validation and characterization of optical redox ratio measurements with a microplate reader in breast cancer cells. SPIE Proceedings. (2015) 9303
7. Walsh AJ, Cook RS, Lee JH, Arteaga CL, Skala MC; Collagen density and alignment of responsive and resistant trastuzumab-treated breast cancer xenografts. Journal of Biomedical Optics. (2015) Feb. 20(2):26004
8. Walsh AJ, Skala MC. Optical metabolic imaging quantifies heterogeneous cell populations. Biomedical Optics Express, (6)2:559-573 (2015).
9. TM Cannon, AT Shah, AJ Walsh, and MC Skala. High-throughput measurements of the optical redox ratio using a commercial microplate reader. Journal of Biomedical Optics. 20(1):010503 (2015).

Presentations:
1. MC Skala, "Metabolic imaging of cancer," Telluride Science Research Conference, Telluride, CO (August 2015)
2. MC Skala, "Multiphoton autofluorescence imaging of metabolism for drug development and treatment planning in cancer," OSA CLEO: Europe. Munich Germany (June 2015)
3. MC Skala, "Fluorescence lifetime imaging of cellular heterogeneity in cancer drug response," OSA CLEO. San Jose, CA (May 2015)
4. MC Skala, "Nonlinear Microscopy of Cellular Metabolism," OSA Topical Meeting: Novel Techniques in Microscopy. Vancover Canada (April 2015)
5. MC Skala, "New methods for assessing cellular metabolic heterogeneity," AACR-SNMMI Joint Conference on Molecular Imaging. San Diego, CA (February 2015)
6. MC Skala, "Fluorescence lifetime imaging of cellular metabolic heterogeneity in cancer," Advanced Imaging Workshop. University of California, Berkeley. (February 2015)
7. AJ Walsh, RS Cook, ME Sanders, CL Arteaga, MC Skala, "Optical metabolic imaging predicts drug response in primary-tumor derived organoids." Gordon Research Conference: Lasers in Medicine and Biology. July 2014. Poster Presentation. **Poster Award.**
8. MC Skala, AJ Walsh, RS Cook, ME Sanders, CL Arteaga. "Cellular-Level Metabolic Imaging to Predict Anti-Cancer Drug Response." Gordon Research Conference: Lasers in Medicine and Biology. July 2014. Podium Presentation.
9. AJ Walsh, ME Sanders, RS Cook, MC Skala. "Fluorescence Lifetime Imaging Classifies Breast Cancer Subtypes and Predicts Neoadjuvant Therapy Response in Humans." SPIE Photonics West, San Francisco, California. February 2014. Podium Presentation.
10. AJ Walsh, RS Cook, MC Skala, "Fresh versus frozen tissue preparations for quantitative fluorescence lifetime imaging of metabolic NADH and FAD." SPIE Photonics West, San Francisco, California. February 2014. Podium Presentation.
11. MC Skala. "Metabolic Imaging of Cancer Drug Response." Advanced Imaging Workshop, University of California, Berkeley, CA. January 2014. Podium Presentation.
12. MC Skala. "Optical Metabolic Imaging of Drug Efficacy in Cancer." 7th Annual Workshop on Advanced TCSPC Techniques, Bethesda MD. October 2013. Podium Presentation.

CONCLUSION
These results indicate that OMI in primary breast tumor organoids can provide early, sensitive measures of treatment response. This system can therefore be used to streamline pre-clinical drug development, by reducing the number of animals, cost, and time required to screen new drugs and drug combinations. The feasibility of OMI measurements in organoids derived from primary human breast tumors has also been demonstrated, with the exciting possibility of providing individualized drug screens in patients before the patient is ever treated. This personalized drug planning approach could reduce toxicities of ineffective treatments, and enable improved outcomes through early, effective interventions. The single-cell analysis capabilities of this technique also have the potential to identify drug combinations that will eliminate treatment-resistant sub-populations of cells that are likely to cause metastases.

REFERENCES

1.   Walsh, A.J., R.S. Cook, M.E. Sanders, L. Aurisicchio, G. Ciliberto, C.L. Arteaga, and M.C. Skala, *Quantitative optical imaging of primary tumor organoid metabolism predicts drug response in breast cancer.* Cancer Res, 2014. Sep 15;74(18):5184-5194.

APPENDICES

1. AJ Walsh, RS Cook, ME Sanders, L Aurisicchio, G Ciliberto, CL Arteaga, and MC Skala. Quantitative optical imaging of primary tumor organoid metabolism predicts drug response in breast cancer. Cancer Research (2014), Sep 15;74(18):5184-5194.

2. AJ Walsh, RS Cook, HC Manning, DJ Hicks, A Lafontant, CL Arteaga, and MC Skala. Optical metabolic imaging identifies breast cancer glycolytic levels, sub-types, and early treatment response. Cancer Research (2013)Oct 15;73(20):6164-74.

SUPPORTING DATA

See main text and attached papers.

Cancer Research

Optical Metabolic Imaging Identifies Glycolytic Levels, Subtypes, and Early-Treatment Response in Breast Cancer

Alex J. Walsh, Rebecca S. Cook, H. Charles Manning, et al.

Updated version	Access the most recent version of this article at: http://cancerres.aacrjournals.org/content/73/20/6164

Cited Articles	This article cites by 48 articles, 25 of which you can access for free at: http://cancerres.aacrjournals.org/content/73/20/6164.full.html#ref-list-1

E-mail alerts	Sign up to receive free email-alerts related to this article or journal.
Reprints and Subscriptions	To order reprints of this article or to subscribe to the journal, contact the AACR Publications Department at pubs@aacr.org.
Permissions	To request permission to re-use all or part of this article, contact the AACR Publications Department at permissions@aacr.org.

Optical Metabolic Imaging Identifies Glycolytic Levels, Subtypes, and Early-Treatment Response in Breast Cancer

Alex J. Walsh[1], Rebecca S. Cook[2,5], H. Charles Manning[1,4], Donna J. Hicks[2], Alec Lafontant[1], Carlos L. Arteaga[2,3,5], and Melissa C. Skala[1]

Abstract

Abnormal cellular metabolism is a hallmark of cancer, yet there is an absence of quantitative methods to dynamically image this powerful cellular function. Optical metabolic imaging (OMI) is a noninvasive, high-resolution, quantitative tool for monitoring cellular metabolism. OMI probes the fluorescence intensities and lifetimes of the autofluorescent metabolic coenzymes reduced NADH and flavin adenine dinucleotide. We confirm that OMI correlates with cellular glycolytic levels across a panel of human breast cell lines using standard assays of cellular rates of glucose uptake and lactate secretion ($P < 0.05$, $r = 0.89$). In addition, OMI resolves differences in the basal metabolic activity of untransformed from malignant breast cells ($P < 0.05$) and between breast cancer subtypes ($P < 0.05$), defined by estrogen receptor and/or HER2 expression or absence. *In vivo* OMI is sensitive to metabolic changes induced by inhibition of HER2 with the antibody trastuzumab (herceptin) in HER2-overexpressing human breast cancer xenografts in mice. This response was confirmed with tumor growth curves and stains for Ki67 and cleaved caspase-3. OMI resolved trastuzumab-induced changes in cellular metabolism *in vivo* as early as 48 hours posttreatment ($P < 0.05$), whereas fluorodeoxyglucose-positron emission tomography did not resolve any changes with trastuzumab up to 12 days posttreatment ($P > 0.05$). In addition, OMI resolved cellular subpopulations of differing response *in vivo* that are critical for investigating drug resistance mechanisms. Importantly, OMI endpoints remained unchanged with trastuzumab treatment in trastuzumab-resistant xenografts ($P > 0.05$). OMI has significant implications for rapid cellular-level assessment of metabolic response to molecular expression and drug action, which would greatly accelerate drug development studies. *Cancer Res; 73(20); 6164–74. ©2013 AACR.*

Introduction

Cellular metabolism produces energy and macromolecules necessary for cell survival. Abnormal metabolism is involved in many of the diseases that cause the greatest burden of morbidity and mortality in the developed world. Many malignant cancer cells maintain high rates of glycolysis in the presence of oxygen (1) and oncogenic transformation is linked with changes in metabolic rates. For example, the HER2 receptor tyrosine kinase, which is amplified in about 20% of invasive breast cancer, potently activates the phosphatidylinositol-3 kinase (PI3K)/Akt/mTOR pathway, a master regulator of glucose metabolism (2, 3). Patients with HER2 gene-amplified breast cancers present with more aggressive disease and generally have a poor prognosis (4). HER2 inhibitors such as the antibody trastuzumab (herceptin) provide substantial clinical benefits. However, the action of HER2 inhibitors is limited because of innate and acquired drug resistance (5).

Clinically and in preclinical drug development, there is a need for high-resolution, noninvasive, functional imaging tools to monitor and predict drug efficacy versus lack of efficacy. In cancer research, the primary endpoint of drug efficacy is tumor regression. However, cellular and molecular changes precede changes in tumor size. If these molecular endpoints could be identified and measured, they would provide biomarkers predictive of drug response or drug resistance. Cellular metabolism is particularly sensitive to upstream molecular interventions and therefore may be a powerful biomarker of early-drug response. The HER2 inhibitor trastuzumab, for example, inhibits PI3K-mediated glucose metabolism (6–8). Current preclinical and clinical methodologies to assess metabolic state in tumors *in situ* include fluorodeoxyglucose-positron emission tomography (FDG-PET), immunohistochemical (IHC) assessment of levels of metabolic regulators, and metabolic flux analyses (7, 9–13). Yet each of these techniques fails to capture dynamic changes in metabolic state and poorly reflect sensitivity to drug efficacy (7, 9, 14–18).

Authors' Affiliations: Departments of [1]Biomedical Engineering, [2]Cancer Biology, [3]Medicine, [4]Vanderbilt University Institute of Imaging Science, and [5]Breast Cancer Research Program, Vanderbilt-Ingram Cancer Center, Vanderbilt University Nashville, Tennessee

American Association for Cancer Research

Optical metabolic imaging (OMI) exploits the autofluorescent properties of reducedNADH and flavin adenine dinucleotide (FAD), two metabolic coenzymes. We use multiphoton fluorescence and time-correlated single photon counting to measure the optical redox ratio and fluorescence lifetimes of NADH and FAD in living cells and tissues. The optical redox ratio is the ratio of NADH fluorescence intensity divided by FAD fluorescence intensity (19) and provides a dynamic measure of cellular metabolism (8, 19–21). The fluorescence lifetime, the time a molecule remains in the excited state, is independent of inter- or intrainstrument variability, resolves free and bound protein configurations, and is influenced by preferred protein-binding of the molecules and proximity to quenchers (e.g., oxygen; ref. 22). NADH and FAD each have two-component fluorescence decays. For NADH, the short lifetime (τ_1) corresponds to NADH free in solution, whereas the long lifetime (τ_2) corresponds to protein-bound NADH (23). Conversely, protein-bound FAD corresponds to the short lifetime, whereas free FAD corresponds with the long lifetime (24). The shorter fluorescence lifetimes of both protein-bound FAD and free NADH are due to dynamic quenching by the adenine moiety (22, 25). The mean fluorescence lifetime (τ_m) is the weighted average of the short and long lifetime components, $\tau_m = \alpha_1\tau_1 + \alpha_2\tau_2$, where α_1 and α_2 are the fractional contributions of the short and long lifetimes, respectively.

The images acquired by OMI provide sufficient resolution and contrast to distinguish the cellular and extracellular tissue compartments, as the collagen-enriched ECM generates a strong second harmonic signal that has a lifetime and spectral emission distinct from cellular NADH and FAD (26). Resolution is adequately high to isolate single cells, allowing identification of inflammatory infiltrates in the stroma and tumor epithelia. This single cell-level resolution may be useful for identifying resistant subpopulations of cells that preexist in the tumor and are responsible for cancer relapse.

Because OMI is inexpensive, fast, and directly measures dynamic changes in cellular metabolism that reflect glycolysis, oxidative phosphorylation, and metabolic enzyme microenvironment interactions, we investigated the potential of OMI as a tool for monitoring metabolic response to targeted therapies in human breast cancer cells and xenografts. OMI was validated by measuring metabolic inhibition by cyanide, and in comparison with standard assays of glycolytic metabolism. The sensitivity of OMI to breast cancer subtypes was confirmed. Finally, the OMI-measured response of mouse xenograft models treated with trastuzumab was compared with FDG-PET, IHC, and tumor size measurements. This work represents a significant advancement in the tools available to study cellular metabolism and tumor response to treatment in living systems.

Materials and Methods

Fluorescence lifetime instrumentation

A custom built, commercial multiphoton fluorescence microscope (Prairie Technologies) was used to acquire fluorescence images. A 40X water-immersion objective (1.15 NA) or a 40X oil-immersion objective (1.3 NA) coupled the excitation and emitted light through an inverted microscope (TiE, Nikon). A titanium:sapphire laser (Coherent Inc.) was tuned to 750 nm for excitation of NADH and 890 nm for FAD excitation. The average laser power was 7.5 to 7.8 mW for NADH and 8.4–to 8.6 mW for FAD. A pixel dwell time of 4.8 μs was used. A GaAsP PMT (H7422P-40, Hamamatsu) detected emitted photons. A 400 to 480 nm bandpass filter isolated NADH fluorescence. A 500 nm high pass dichroic mirror and a 500 to 600 nm bandpass filter isolated FAD fluorescence.

Fluorescence lifetime images were acquired using time correlated single photon counting (TCSPC) electronics (SPC-150, Becker and Hickl). TCSPC uses a fast detector PMT to measure the time between a laser pulse and fluorescence event. Each image of 256 × 256 pixels was acquired using an integration time of 60 seconds. No change in the photon count rate was observed, ensuring that photobleaching did not occur. The instrument response function (measured from the second harmonic generated signal of urea crystals excited at 900 nm) full width at half maximum was measured to be 260 ps. The single-component fluorescence lifetime of a fluorescent bead (Polysciences Inc.) was measured daily. The measured fluorescence lifetime of the bead was 2.1 ± 0.08 ns ($n = 18$), which is consistent with published studies (20, 27).

Cell culture

All cell lines were acquired from the American Type Culture Collection except the HR6 cell line (28), which was provided by the Arteaga Laboratory. The noncancerous mammary epithelium cell line, MCF10A, was cultured in MEBM (Lonza) supplemented with cholera toxin, penicillin: streptomycin, bovine pituitary extract, hydrocortisone, insulin, and human epidermal growth factor. All malignant cell lines were grown in DMEM (Invitrogen) with 10% FBS and 1% penicillin: streptomycin. The growth media for the HR6 cell line was further enhanced with 25 μg/mL trastuzumab (Vanderbilt Pharmacy). For fluorescence imaging, cells were plated at a density of 10^6 cells per 35 mm glass-bottom imaging dish (MatTek Corp.) 48 hours before imaging.

The MCF10A cell line was used as a daily fluorescence standard for the redox ratio and imaged each day measurements were acquired. All other cell lines were imaged on at least two different days. A total of 18 different locations were imaged for each cell line (58 for MCF10A cells) from six different dishes (three images were acquired from each dish, see Supplementary Table S1).

Cyanide experiment

NADH and FAD fluorescence lifetime images of three locations of three dishes were acquired. Media of two of the MCF10A dishes was removed and replaced with cyanide supplemented MCF10A growth media (4 mmol/L NaCN, Sigma). The cells were allowed 5 minutes for the cyanide to react and post-cyanide NADH and FAD fluorescence images were acquired from three unique locations from each dish.

Trastuzumab perturbation

The effect of HER2 inhibition by trastuzumab was tested in HER2-overexpressing cells. The cells were plated at a density of

10^6 cells per imaging dish, 48 hours before imaging. At 24 hours before imaging, the growth media was exchanged for growth media containing 25 μg/mL trastuzumab. This dose of trastuzumab, 25 μg/mL, was chosen to mimic therapeutic drug dosage in patients (29).

Mouse xenografts

This study was approved by the Vanderbilt University Animal Care and Use Committee and meets the NIH guidelines for animal welfare. MDA-MB-361 cells (10^6), BT474 cells (10^8), or HR6 cells (10^8) in 100 μL Matrigel were injected in the inguinal mammary fat pads of female athymic nude mice (J:NU; Jackson Laboratories). Tumors were allowed to grow to approximately 150 mm^3. Tumor-bearing mice were treated with trastuzumab (Vanderbilt University Medical Center pharmacy) or control human immunoglobulin G (IgG) 10 mg/kg twice weekly for two weeks. This dose of trastuzumab was chosen to mimic therapeutic drug dosage in patients (30).

OMI xenograft imaging

Isoflurane-anesthetized mice were used for vital imaging, by removing the skin overlying the tumor, overlaying the tumor with a coverslip, and placing the mouse on the microscope stage. NADH and FAD fluorescence lifetime images of three different tumor locations were acquired each day. After imaging, mice were humanely euthanized while under anesthesia. Each OMI group contained 3 mice, each with 2 tumors for a total n of 6 tumors at each time point.

FDG-PET imaging

The FDG-PET protocol follows published methods (7, 31, 32). The mice were fasted overnight and allowed to acclimate to the PET facility for 1 hour on a warm water pad. A single retroorbital injection of approximately 200 μCi (100 μL) of [^{18}F]FDG was administered. Following a 40-minute distribution period, 20-minute static PET scans were collected on a Concorde Microsystems microPET Focus 220 (Siemens), whereas mice were anesthetized with isoflurane. PET images were reconstructed using the ordered subsets expectation maximization algorithm (33). FDG-uptake values were obtained by isolating the uptake of each tumor volume and correcting for the injected dose. Each FDG-PET group contained 5 mice, each with 2 tumors for a total n of 10 tumors.

Quantification of the optical redox ratio

The optical redox ratio was computed from the NADH and FAD fluorescence lifetime data. The photons detected at each pixel in an image were integrated over time to compute the sum of photons per pixel. The total number of NADH photons was divided by the total number of FAD photons at each pixel to create a redox ratio image (MATLAB, MathWorks). The redox ratio image was thresholded to remove background and nuclear fluorescence and the average redox ratio for the remaining cell cytoplasms was computed. This approach has been confirmed to be consistent with redox ratios obtained with steady-state detection (8, 21).

Quantification of fluorescence lifetime components

For each image, a threshold was selected to eliminate background and nuclear fluorescence (SPCImage, Becker and Hickl). A binning of nine surrounding pixels was used. Then, the fluorescence lifetime components were computed for each pixel by deconvolving the measured system response and fitting the resulting exponential decay to a two-component model, $I(t) = \alpha_1 \exp^{-t/\tau_1} + \alpha_2 \exp^{-t/\tau_2} + C$, where $I(t)$ is the fluorescence intensity at time t after the laser excitation pulse, α_1 and α_2 are the fractional contributions of the short and long lifetime components, respectively (i.e., $\alpha_1 + \alpha_2 = 1$), τ_1 and τ_2 are the fluorescence lifetimes of the short and long lifetime components, and C accounts for background light. A two-component decay was used to represent the lifetimes of the free and bound configurations of NADH and FAD (20, 23, 24). The average lifetime component values and a mean fluorescence lifetime ($\tau_m = \alpha_1 \tau_1 + \alpha_2 \tau_2$) for each image were computed in MATLAB.

Statistical analysis

A rank sum test of means was used to test for significant differences due to cyanide. A Bonferroni correction for multiple-comparisons was used on rank sum tests of means of the metabolic values from the panel of cell lines. A rank sum test of means was used to identify significant differences when cell lines were treated with trastuzumab and to find differences in the *in vivo* xenograft experiments. A Student t test of means tested for significantly different FDG-uptake values between control and trastuzumab-treated xenografts. For all statistical tests, an $\alpha_{significance}$ level of 0.05 was used and the test was assumed to be two-way.

Spearman rank correlation coefficient was used to identify correlations. Both a correlation coefficient (r) and a P value were computed. An α level of less than 0.05 signified significance. Scatterplots of the significant correlations confirmed that the correlation was due to data trends and not a single outlier.

Computation of intra- and intercellular variation

Intercellular variation was visualized by histogram representation of the mean metabolic measure (optical redox ratio, NADH τ_m, or FAD τ_m) for all cells. The histogram was fit to one, two, and three component Gaussian curves to determine the number of modes within the data. The fit with the lowest Akaike information criterion was selected to represent the probability density function of the histogram (34). Intracellular variation was computed as the average coefficient of variation (SD divided by mean) for each cell and averaged over all cells.

Percentage of mitotic cells

The percentage of proliferating cells was measured by flow cytometry. Cells were plated at a density of 10^6 cells per 35 mm dish. After 48 hours, the cells were labeled with Phospho-Histone H3 (Ser10) antibody (Cell Signaling Technology) and a secondary antibody, Alexa Fluor 488 goat anti-rabbit IgG (Invitrogen) enabled detection of labeled cells by flow cytometry.

Glycolytic index

Media glucose and lactate concentrations were measured using standard assay kits [Amplex Red Glucose/Glucose Oxidase Assay Kit (Invitrogen) and L-Lactate Assay Kit (Eton Bioscience Inc.)]. Concentrations of glucose and lactate in the cell growth media were determined at the time of plating (0 hour) and at the time of imaging (48 hour). The "glycolytic index" was computed as the moles of glucose consumed within 48 hours divided by the moles of lactate produced in 48 hours.

Histologic analysis

Tumors were collected and placed in buffered formalin, paraffin embedded, sliced, and stained with hematoxylin and eosin stain. Additional slides were stained for Ki-67 and cleaved caspase-3. Staining protocols were verified in positive control samples. The percentage of positively stained cells was quantified from five fields of view from three tumors in each group.

Results

Figure 1A shows the relationship between HER2 and the fluorescent molecules NADH and FAD. HER2 activation drives an increase in glycolysis, which generates NADH. The pyruvate produced in glycolysis can enter the mitochondria as a reactant in oxidative phosphorylation. Oxidative phosphorylation consumes NADH and produces FAD. A net gain of NADH relative to FAD is observed with HER2 activation due to a relative increase in glycolysis.

Validation

Chemical inhibition of oxidative phosphorylation affects the relative fluorescence intensities of NADH and FAD in a cell (35), so this perturbation was used to validate the optical imaging approach (Fig. 1B–D, Supplementary Fig. S1). Cyanide (which disrupts the electron transport chain) induced the predicted trends 23, 27): an increase in the optical redox ratio and a decrease in NADH τ_m. Unreported until now, FAD τ_m increased with cyanide treatment.

Metabolic profiling of breast cancer cells

High-resolution images (Fig. 2) allowed visualization of cellular morphology and cell-to-cell variability of the optical redox ratio and NADH and FAD fluorescence lifetimes for human breast cell lines (Supplementary Table S1). Cellular fluorescence localized to the cytoplasm of cells. $ER^+/HER2^-$ cells displayed increased redox ratios over that seen in triple-negative cells ($P < 0.001$; Fig. 3A), and the greatest redox ratios were measured in HER2 gene-amplified cells ($P < 0.001$). To account for any differences in cellular proliferation rates among the cell lines and show that the redox ratio is not a reporter of cellular proliferation (Supplementary Fig. S2A), we normalized the redox ratio to the percentage mitotic cells (Supplementary Fig. S2B) and found similar trends, increased redox ratio/percentage mitotic cells in ER^+ cells and the greatest redox ratio/percentage mitotic cells in $HER2^+$ cells.
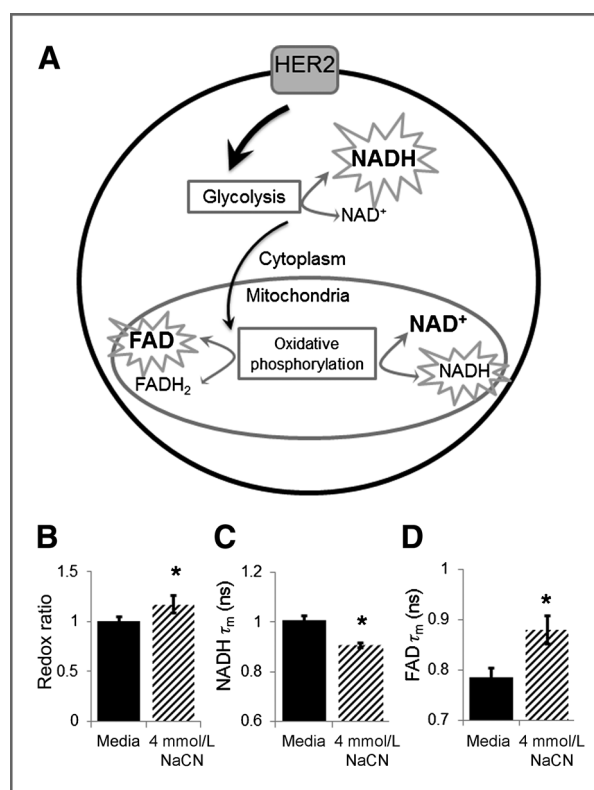

Figure 1. A, graphical representation of the relationship between HER2, NADH, and FAD. HER2 activation drives an increase in glycolysis, which produces NADH. The pyruvate generated in glycolysis can enter the mitochondria as a reactant in oxidative phosphorylation. Oxidative phosphorylation consumes NADH and produces FAD. A net gain of NADH relative to FAD is observed with HER2 activation due to a relative increase in glycolysis. Inhibition of HER2 by trastuzumab reduces cellular glycolysis rates, resulting in a decrease of cellular NADH relative to FAD. NADH and FAD are highlighted as the fluorescent molecules in this diagram and molecules in bold indicate the net direction of the reaction. Optical redox ratio (B), NADH τ_m (C), and FAD τ_m (D) of MCF10A (nonmalignant) cells before ($n = 9$) and after ($n = 6$) treatment with 4 mmol/L NaCN. τ_m is the mean lifetime ($\tau_m = \tau_1{}^*\alpha_1 + \tau_2{}^*\alpha_2$). *, $P < 0.05$.

NADH τ_m of $HER2^+$ and ER^+ cells were increased over that measured in nonmalignant cells ($P < 0.001$; Fig. 3B), but were statistically similar to each other ($P = 0.5$). Triple-negative cells exhibited the shortest NADH τ_m. Reduced-free and protein-bound NADH lifetimes (τ_1 and τ_2) were observed in the triple-negative and ER^+ cells (Supplementary Fig. S3A and S3B). The portion of free NADH (α_1) was decreased in the $HER2^+$ cells compared with the nonmalignant cells (Supplementary Fig. S3C). Compared with nonmalignant cells, FAD τ_m was increased in all malignant cells ($P < 0.001$), with the longest FAD τ_m observed in $ER^+/HER2^-$ cells ($P < 0.001$; Fig. 3C). Increased FAD τ_1 and τ_2 values, as well as a reduced α_1 (contribution of bound FAD) contributed to the increased FAD τ_m observed in the malignant cells (Supplementary Fig. S3D–S3F). A scatterplot of NADH τ_m versus redox ratio/percentage mitotic cells (Fig. 3D) allowed accurate clustering of data-points of nonmalignant, triple-negative, ER^+, and $HER2^+$ cells. Scatterplots of FAD τ_m versus redox ratio and
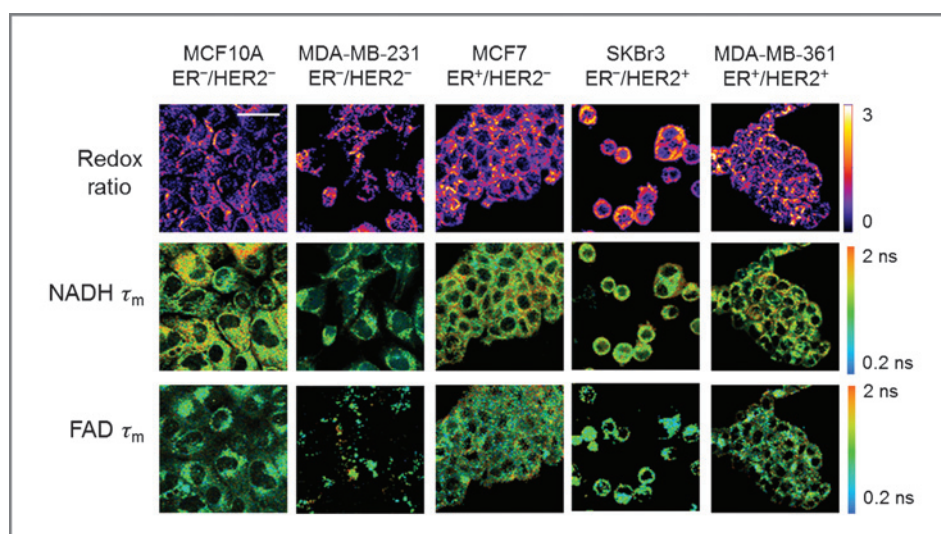
Figure 2. Representative images of the optical redox ratio (NADH/FAD; first row), NADH τ_m (second row), and FAD τ_m (third row) of MCF10A (nonmalignant) and malignant breast cells. Scale bar, 30 μm. The redox ratio is normalized to the mean daily MCF10A mean redox ratio as a daily fluorescence standard. τ_m is the mean lifetime ($\tau_m = \tau_1{}^*\alpha_1 + \tau_2{}^*\alpha_2$). The ER and HER2 status of each cell line is provided under its name.

NADH τ_m versus FAD τ_m allow separation of triple-negative and nonmalignant cells (Supplementary Fig. S4).

We compared OMI with cellular rates of glucose uptake and lactate secretion or the "glycolytic index." A Spearman rank correlation coefficient (r) of 0.89 ($P < 0.05$) defined a positive correlation between the optical redox ratio/percentage mitotic cells and the glycolytic index (Fig. 3E). Neither NADH τ_m nor FAD τ_m correlated with the glycolytic index or the redox ratio (Supplementary Table S2).

Trastuzumab response *in vitro*

The effect of trastuzumab on cellular metabolism was investigated in three HER2-overexpressing cell lines: BT474 cells that are responsive to trastuzumab, MDA-MB-361
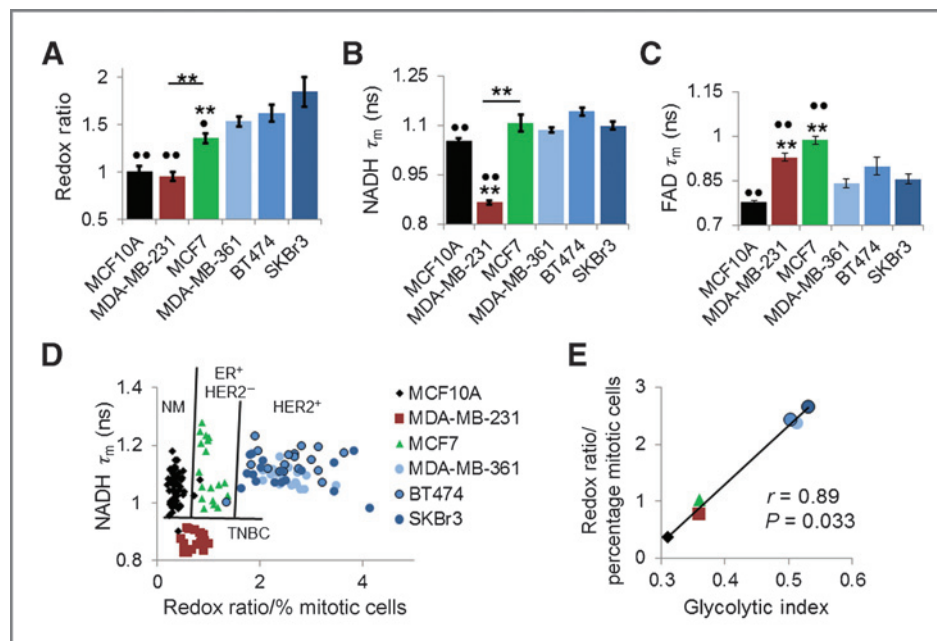

Figure 3. A, the optical redox ratio (mean ± SE) is increased in malignant cells with ER overexpression (MCF7, green) and is further increased in cells with HER2 overexpression (MDA-MB-361, BT474, and SKBr3; blue). B, the NADH τ_m (mean ± SE) is decreased in triple-negative cells (MDA-MB-231, red) relative to nonmalignant, ER$^+$, and HER2$^+$ cells. The NADH τ_m is increased in HER2$^+$ cells relative to nonmalignant cells. C, FAD τ_m (mean ± SE) is increased in malignant cells relative to nonmalignant cells. D, a scatterplot of NADH τ_m versus redox ratio/percentage mitotic cells provides visual separation of the different molecular subtypes of breast cancer [nonmalignant (NM), ER$^+$/HER2$^-$, HER2$^+$, and triple-negative (TNBC)]. E, correlation between redox ratio/percentage mitotic cells and glycolytic index. Unless indicated with a line, asterisks (*) indicate statistically significant differences with the MCF10A (nonmalignant) cells and bullets (•) indicate statistically significant differences with the HER2$^+$ cells grouped together. **, $P < 0.001$. $n = 18$ for all malignant cell lines and $n = 58$ for MCF10A.
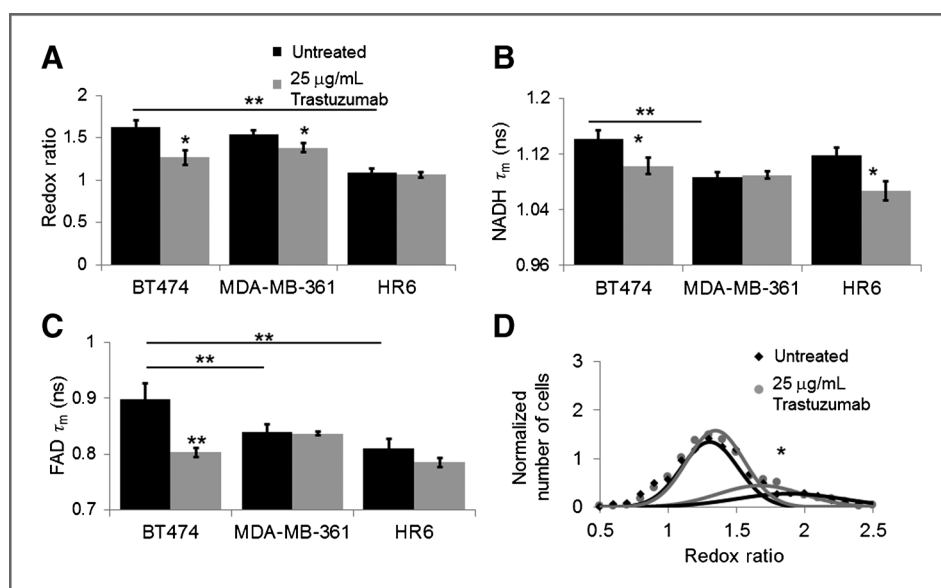
Figure 4. A, the redox ratio (mean ± SE) decreases with trastuzumab treatment in responsive (BT474) and partially responsive (MDA-MB-361) cells but remains unchanged in cells with acquired resistance to trastuzumab (HR6). B, NADH τ_m (mean ± SE; $\tau_m = \tau_1^* \alpha_1 + \tau_2^* \alpha_2$) is shorter in trastuzumab-treated responsive cells (BT474) and cells with acquired resistance (HR6), but unchanged in cells with poor response (MDA-MB-361). C, FAD τ_m (mean ± SE) is shorter in trastuzumab-treated BT474 but unchanged MDA-MB-361 and HR6 cells. *, significance between control and treated, unless otherwise indicated. D, distribution density modeling (black line, fit of untreated cell histogram; gray line, fit of trastuzumab-treated cells) of the redox ratio on a cell-by-cell basis reveals two distinct populations of MDA-MB-361 cells for the redox ratio, with 70% and 30% of cells in the majority and minority populations, respectively, for both control and treated cells. There is a significant decrease ($P < 0.05$) in the mean of the minority population of treated cells (but not in the majority population), suggesting trastuzumab response in a subpopulation of cells. **, $P < 0.001$; *, $P < 0.05$. $n = 18$ images for control and treated for all cell lines.

cells that partially respond to trastuzumab, and HR6 cells, which were derived from a BT474 xenograft that acquired resistance to trastuzumab *in vivo* (28). The redox ratio ($P < 0.05$), NADH τ_m ($P < 0.05$), and FAD τ_m ($P < 0.001$) of BT474 cells decreased upon trastuzumab treatment for 24 hours (Fig. 4A–C). Lifetime component analysis showed significant increases in the portions of free NADH (α_1) and bound FAD (α_1) of BT474 cells treated with trastuzumab (Supplementary Fig. S5). Similarly, the redox ratio of the MDA-MB-361 cells decreased ($P < 0.05$) with trastuzumab treatment (Fig. 4A). The high-resolution OMI enabled analysis of cellular heterogeneity in response to trastuzumab (Fig. 4D, Supplementary Fig. S6). Distribution modeling of cellular redox ratios of MDA-MB-361 cells revealed two subpopulations characterized by differing redox ratios (Fig. 4D). The mean redox ratio of the first population, representing 70% of cells, showed no change (1.34 to 1.31) upon trastuzumab treatment ($P = 0.07$), suggesting that trastuzumab did not affect metabolic processes in the majority of MDA-MB-361 cells. However, 30% of the cells responded to trastuzumab with a mean redox ratio that decreased from 1.89 to 1.65 ($P < 0.001$).

HR6 cells are a trastuzumab-resistant BT474-derived subline that retains HER2 overexpression. Previous studies have shown maintenance of HER2 overexpression and PI3K/Akt signaling in trastuzumab-treated HR6 cells (28). Consistent with this observation, the redox ratio remained unchanged upon treatment with trastuzumab, as was FAD τ_m. NADH τ_m decreased in HR6 cells upon treatment with the antibody ($P < 0.05$; Fig. 4A–C). An increased portion of free NADH (α_1) contributed to the decreased NADH τ_m observed in the HR6 cells (Supplementary Fig. S5).

In vivo xenografts

To verify the OMI response observed in cultured cells, we conducted OMI on HER2-overexpressing xenografts and compared these findings with tumor size, IHC, and FDG-PET measurements. Established BT474 xenografts treated with control IgG continued to grow throughout the course of the experiment while the trastuzumab-treated tumors decreased in size (Fig. 5A). IHC staining confirmed lower rates of proliferation and higher rates of apoptosis in the trastuzumab-treated group (Fig. 5B and C). A representative FDG-PET image displays the location of the tumors in the mammary fat near the hind limbs and shows increased FDG-uptake in the tumors compared with the surrounding tissue (Fig. 5D). FDG-uptake increased in the control mice between days 2 and 12 posttreatment; however, no difference was observed between control and trastuzumab-treated tumors at any time point (day 2, 5, or 12 posttreatment; Fig. 5E). OMI imaging of an identical cohort of tumors allowed cellular-level visualization of metabolism (Fig. 5F) and resolved metabolic differences in the redox ratio (Fig. 5G), NADH τ_m (Fig. 5H, Supplementary Fig. S7A–S7C), and FAD τ_m (Fig. 5I, Supplementary Fig. S7) between control and trastuzumab-responding tumors as early as 2 days after the first dose of trastuzumab.

Tumor size measurements of the HR6 xenografts showed similar growth of both control and trastuzumab-treated HR6
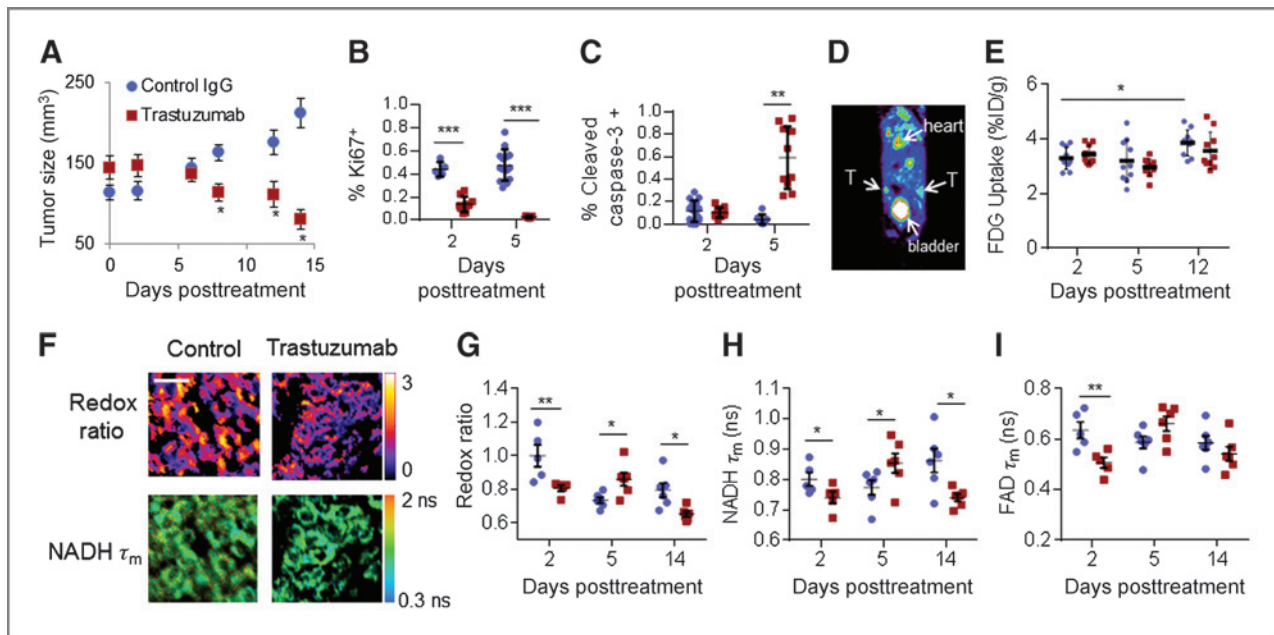
Figure 5. A, BT474 tumors treated with trastuzumab (10 mg/kg, 2× weekly) decrease in size (mean ± SE) compared with control IgG-treated tumors. Trastuzumab versus control at each time point. B, Ki67 staining shows reduced proliferation in trastuzumab-treated tumors. C, cleaved caspase-3 staining shows increased apoptosis in trastuzumab-treated tumors at day 5. D, representative FDG-PET image (T, tumor). E, FDG-uptake increases in control tumors at day 12 compared with control tumors at day 2. No significant difference in FDG-uptake between trastuzumab-treated and control tumors is observed. $n = 10$. F, representative OMI images. Scale bar, 50 μm. G, decreased redox ratio, NADH τ_m (H), and FAD τ_m (I) are observed in trastuzumab-treated tumors at 2 days after trastuzumab-treatment. *, $P < 0.05$, **, $P < 0.01$; ***, $P < 0.001$; $n = 6$ tumors.

tumors (Fig. 6A). IHC confirmed that the trastuzumab-treated HR6 tumors retain proliferative capabilities and express similar rates of apoptosis compared with control-treated tumors (Fig. 6B and C). A representative FDG-PET image of the HR6 tumors shows increased FDG-uptake by the tumor compared with the surrounding tissue (Fig. 6D). No change in FDG-PET
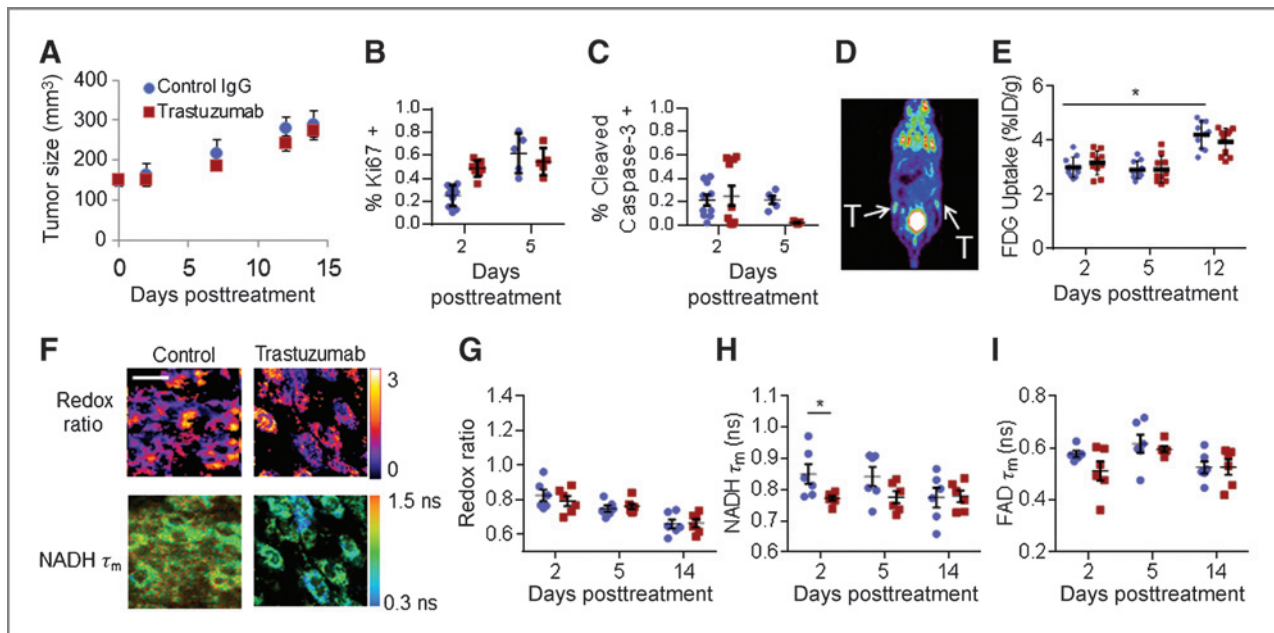

Figure 6. A, HR6 tumor size (mean ± SE) treated with trastuzumab (10 mg/kg, 2× weekly) compared with control IgG-treated tumors. B, Ki67 staining of HR6 control IgG and trastuzumab-treated tumors. C, cleaved caspase-3 staining of HR6 control IgG and trastuzumab-treated tumors. D, representative FDG-PET image (T, tumor). E, FDG-uptake increases in control tumors at day 12 compared with control tumors at day 2, *, $P < 0.05$. No significant difference in FDG-uptake between trastuzumab-treated and control tumors is observed at any time. $n = 10$. F, representative OMI images; scale bar, 50 μm. G, redox ratio, NADH τ_m (H), and FAD τ_m (I) of control and trastuzumab-treated tumors. *, $P < 0.05$; $n = 6$ tumors.
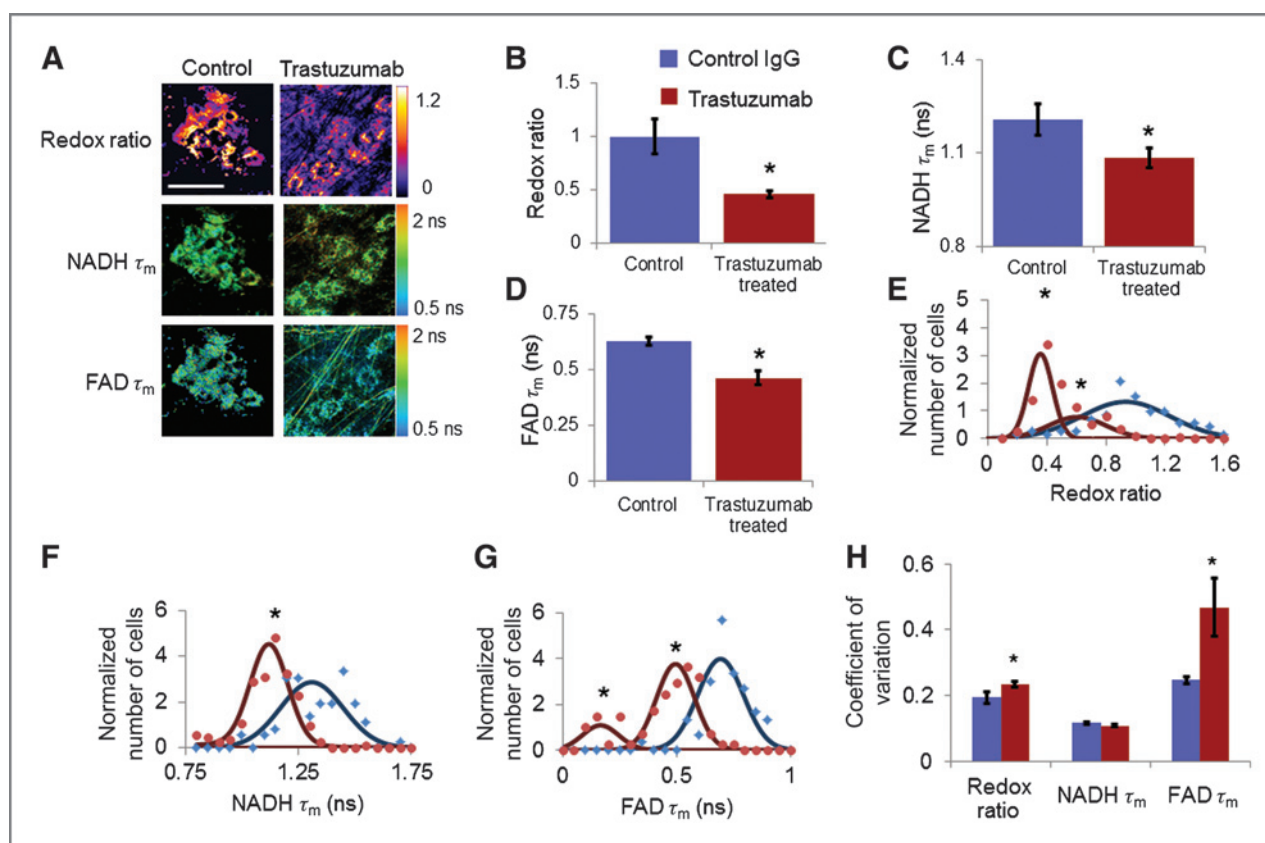
Figure 7. A, representative images of the optical redox ratio (first row), NADH τ_m (second row), and FAD τ_m (third row) of untreated control and trastuzumab-treated (10 µg/kg; 48 hours) MDA-MB-361 mouse xenograft tumors. Fibrillar structures are due to collagen second harmonic generation. Scale bar, 50 µm. B–D, mean ± SE on a per image basis. E–G, distribution density modeling on a cell-by-cell basis in control and trastuzumab-treated tumors. B, the optical redox ratio is reduced in trastuzumab-treated tumors compared with the control tumors. C, NADH τ_m is reduced in the trastuzumab-treated tumors compared with the control tumors. D, FAD τ_m is reduced in trastuzumab-treated tumors compared with the control tumors. E–G, distribution density modeling reveals two distinct populations of trastuzumab-treated cells for the redox ratio (E, maroon line) and FAD τ_m (G, maroon line) measurements, indicating heterogeneous cellular metabolic response to treatment. E–G, blue lines, all control populations and the trastuzumab-treated NADH τ_m population (F, maroon line) are unimodal. H, the increased coefficient of variation in the redox ratio and FAD τ_m of the trastuzumab-treated xenografts indicates increased intracellular variation in metabolism. *, $P < 0.05$.

was observed between control and trastuzumab-treated tumors at any time point; however, the FDG-uptake was increased in the control mice at 12 days compared with 2 days (Fig. 6E). No difference was observed in the redox ratio between control and treated HR6 tumors at any time point (Fig. 6F and G). NADH τ_m decreased in the HR6-treated tumors relative to controls at 2 days posttreatment, but was similar to controls at days 5 and 14 (Fig. 6H, Supplementary Fig. S8). No change in FAD τ_m was observed at any time point (Fig. 6I, Supplementary Fig. S8).

The redox ratio ($P < 0.05$), NADH τ_m ($P < 0.05$), and FAD τ_m ($P < 0.05$) decreased in trastuzumab-treated MDA-MB-361 xenografts as compared with IgG-treated controls (Fig. 7A–D; Supplementary Fig. S9) 2 days after treatment. Modeling of the optical redox ratio and FAD τ_m values on a cell-by-cell basis (intercell variability) identified two subpopulations of tumor cells in trastuzumab-treated animals, whereas an unimodal cellular distribution was identified for NADH τ_m (Fig. 7E–G). High-resolution analysis revealed that intracellular variability in redox ratios and FAD τ_m increased

($P < 0.05$) in trastuzumab-treated samples (Fig. 7H). These results fully characterize OMI and show its potential for monitoring early-drug response in cell culture and mouse xenografts on a single-cell level.

Discussion

OMI is advantageous for live cell and animal imaging due to several features, including direct and dynamic assessment of cellular metabolism *in vivo*, cellular and subcellular resolution imaging capabilities, rapid acquisition, low-cost, use of intrinsic signals (no contrast agents, no radioactivity), and high sensitivity to metabolic changes. Our results have significant implications for rapid assessment of drug action in preclinical models, which would greatly accelerate drug development studies.

These results are the first to correlate OMI with a standard assay of metabolic behavior. Although the optical redox ratio is inferred from theory as the relative rates of glycolysis and oxidative phosphorylation within cells, we confirm a strong

positive correlation ($r = 0.89$, $P = 0.03$) with a standard measure of cellular glycolytic levels (Fig. 3). In contrast, NADH τ_m and FAD τ_m are not correlated with the glycolytic index (Supplementary Table S2). The proportion of free NADH (α_1) has been interpreted as an analog to the optical redox ratio (27); however, we did not find a correlation between the optical redox ratio and NADH α_1 (Supplementary Table S2). Given the physical nature of these fluorescence lifetime measurements, which are sensitive to protein-binding, relative fractions of free and bound components, and proximity to quenchers, it is not surprising that they are sensitive to more cellular processes than just glycolysis. For example, changes in the distribution of NADH and FAD enzyme–binding sites associated with preferred metabolic pathways in breast cancer subtypes may be responsible for the changes in protein-bound lifetimes between cell lines (36). The changes in the lifetimes of the free components of NADH and FAD may reflect changes in dynamic quenching (22). Taken together, the data (Fig. 3, Supplementary Table S2) indicate that the redox ratio, NADH, and FAD lifetimes provide independent measures of cellular metabolism and the molecular microenvironment. The varied dynamics of these endpoints due to HER2 inhibition suggest that all three OMI endpoints provide added value when measured together.

We used these tools to differentiate breast cancer cells by subtype, defined by ER, and/or HER2 expression or absence (Fig. 3). OMI is sensitive to metabolic behaviors caused by ER and HER2 (Fig. 3), known oncogenic drivers of glycolytic metabolism in breast cancer cells (3, 8, 37, 38). ER regulates gene expression of glucose transporter proteins and proteins involved in oxidative phosphorylation and the citric acid cycle such as isocitrate dehydrogenase, which actively reduces NAD^+ to NADH (37, 39–41). HER2 mediates metabolism through signaling of the PI3K/Akt/mTOR pathway, which directs transcription of glycolytic enzymes (2, 3). When combined, the redox ratio and NADH lifetime fully separate the distinct subtypes of breast cancer (Fig. 3D), indicating that the complementary measures of the redox ratio and fluorescence lifetime allow robust characterization of cellular metabolism and molecular microenvironments associated with breast cancer subtypes.

We further show that the OMI endpoints optical redox ratio, NADH τ_m, and FAD τ_m, reflect impaired metabolic activity in trastuzumab-responsive BT474 cells (Fig. 4) *in vitro*, suggesting a large metabolic response of HER2-amplified cells to trastuzumab. Only one of the OMI endpoints, NADH τ_m, decreased in the trastuzumab-resistant HR6 cells (Fig. 4). Although HR6 cells maintain HER2-overexpression and PTEN and P-Akt protein levels in the presence of trastuzumab, blockage of HER2 with trastuzumab may affect internal signaling (28). Because of its highly sensitive nature, NADH τ_m may be reporting such minute metabolism differences.

A subset of variables also resolved metabolic changes induced by trastuzumab in poorly responsive HER2-amplified cells (MDA-MB-361) *in vitro* (Fig. 4). Behavioral heterogeneity inherent to the MDA-MB-361 cell line suggests that 25% of the overall population would be growth inhibited by trastuzumab *in vitro* (42). Our data detected a 30% subpopulation

within MDA-MB-361 cells that responded to trastuzumab through decreased redox ratios (Fig. 4D), suggesting correlative evidence that high-resolution optical imaging is capable of detecting responders and nonresponders at the single-cell level in the context of a heterogeneous tumor cell population with a mixed response. The complementary metabolic information gained from the OMI endpoints allowed identification of a large metabolic response to trastuzumab (BT474) but also resolved negative (HR6) and partial (MDA-MB-361) responses, showing high sensitivity and resolution of OMI.

Finally, we measured the *in vivo* metabolic response to trastuzumab in HER2-overexpressing mouse xenografts. Trastuzumab-induced metabolic repression in BT474 and MDA-MB-361 tumors was detected by 48 hours posttreatment (Figs. 5 and 7). The redox ratio and FAD τ_m did not change in trastuzumab-resistant HR6 tumors treated with the antibody (Fig. 6). However, NADH τ_m decreased in trastuzumab-treated HR6 tumors compared with controls at 48 hours (Fig. 6), which was consistent with the *in vitro* results (Fig. 4). Modeling of the intercellular variation of MDA-MB-361 xenograft tumors identified two subpopulations in response to trastuzumab for the optical redox ratio and FAD τ_m (Fig. 7), suggesting *in vivo* cell-to-cell heterogeneity. This heterogeneous *in vivo* response is consistent with the *in vitro* results (in Fig. 4). We attempted to include only tumor cells in our image analysis, by evaluation of the cell morphology with respect to histology, but acknowledge that nontumor cell populations could have been included in this analysis. We speculate the greater intracellular variation of both the redox ratio and FAD τ_m observed in the MDA-MB-361 tumors treated with trastuzumab (Fig. 7H) is due to heterogeneous responses of individual mitochondria (43). Elucidation of this possibility will require additional research.

The tumor size measurements and IHC analysis of cellular proliferation and apoptosis were consistent with an antitumor effect of trastuzumab against BT474 tumors and a lack of an effect against HR6 tumors (Figs. 5 and 6). Tumor size measurements first identified a difference in control versus trastuzumab-treated BT474 tumor size at 8 days after treatment was initiated (Fig. 5A), 6 days later than the first significant change in OMI endpoints between control and trastuzumab-treated tumors (day 2, Fig. 5G). Although Ki67 staining of BT474 tumors identified reduced proliferation in BT474 tumors treated with trastuzumab at 2 and 5 days posttreatment, OMI is advantageous over IHC as a measure of tumor response because OMI provides a dynamic measure of cellular metabolism and can be conducted *in vivo* and over time within the same animal. Although *in vivo* OMI data are presented here, OMI endpoints remain robust measures of metabolism in freshly excised tissues (21) allowing implementation of this metabolic imaging technique in situations when *in vivo* measurements are not feasible.

FDG-PET has also been explored as a potential tool for assessing response to therapeutic agents. Consistent with a prior study (7), in this study, FDG-PET failed to identify a metabolic difference between control and trastuzumab-treated BT474 tumors (Fig. 5). FDG-uptake did increase over time as the control tumors continued to grow. Unlike OMI, PET cannot resolve cellular subpopulations of differing response

that are critical for investigating drug resistance mechanisms (7, 13–17, 44). Furthermore, PET requires large upfront and continued costs due to radiolabeled tracers, whereas OMI can be implemented in low-cost, wide-field, or confocal microscopes without the need for external dyes (45–47). In addition, OMI allows for fast, accurate, dynamic *in vivo* monitoring of early-therapeutic response, potentially reducing time and animals required for drug development. Our studies have focused on breast cancer and HER2 inhibition, but the methods developed are also applicable to the array of diseases that are treated with metabolism-modulating drugs (48–50).

The results of this study validate OMI as a powerful tool for quantifying cellular metabolism, which is an active area of investigation across multiple diseases. As we show using human breast cancer cells and xenografts, optical metabolic measurements are sensitive to distinct tumor cell subtypes. In addition, we present significant findings suggesting that OMI can be used as an early indicator of metabolic response to treatment with a targeted therapy, both in cell culture and *in vivo*. These results represent the culmination of multiple imaging technologies, analysis tools, and their validation with standard assays and FDG-PET. The results in breast cancer cells and xenografts provide the first direct measurements relating cellular metabolism, HER2 expression, HER2 inhibition, and resistance to HER2 inhibitors in live cells and tissues. In addition, these methodologies are potentially broadly applicable outside the cancer and imaging communities, including those in drug development and metabolism research across multiple diseases. Although we see OMI as an immediately powerful tool in preclinical models, it also may directly impact patient care as an adjunct to current practice, either on freshly

excised tissue (21) or through *in vivo* endoscopes adapted for fluorescence imaging.

References

1. Warburg O. On the origin of cancer cells. Science 1956;123:309–14.
2. Plas DR, Thompson CB. Akt-dependent transformation: there is more to growth than just surviving. Oncogene 2005;24:7435–42.
3. Harari D, Yarden Y. Molecular mechanisms underlying ErbB2/HER2 action in breast cancer. Oncogene 2000;19:6102–14.
4. Ross JS, Fletcher JA. The HER-2/neu oncogene in breast cancer: prognostic factor, predictive factor, and target for therapy. Stem Cells 1998;16:413–28.
5. Vogel CL, Cobleigh MA, Tripathy D, Gutheil JC, Harris LN, Fehrenbacher L, et al. Efficacy and safety of trastuzumab as a single agent in first-line treatment of HER2-overexpressing metastatic breast cancer. J Clin Oncol 2002;20:719–26.
6. Yakes FM, Chinratanalab W, Ritter CA, King W, Seelig S, Arteaga CL. Herceptin-induced inhibition of phosphatidylinositol-3 kinase and Akt is required for antibody-mediated effects on p27, cyclin D1, and antitumor action. Cancer Res 2002;62:4132–41.
7. Shah C, Miller TW, Wyatt SK, McKinley ET, Olivares MG, Sanchez V, et al. Imaging biomarkers predict response to anti-HER2 (ErbB2) therapy in preclinical models of breast cancer. Clin Cancer Res 2009;15:4712–21.
8. Walsh A, Cook RS, Rexer B, Arteaga CL, Skala MC. Optical imaging of metabolism in HER2 overexpressing breast cancer cells. Biomed Opt Express 2012;3:75–85.
9. Brown RS, Wahl RL. Overexpression of Glut-1 glucose transporter in human breast cancer. An immunohistochemical study. Cancer 1993;72:2979–85.
10. Wang L, Zhang Q, Zhang J, Sun S, Guo H, Jia Z, et al. PI3K pathway activation results in low efficacy of both trastuzumab and lapatinib. BMC Cancer 2011;11:248.
11. Zhang D, Tai LK, Wong LL, Chiu LL, Sethi SK, Koay ES. Proteomic study reveals that proteins involved in metabolic and detoxification pathways are highly expressed in HER-2/neu-positive breast cancer. Mol Cell Proteomics 2005;4:1686–96.
12. Nguyen QD, Perumal M, Waldman TA, Aboagye EO. Glucose metabolism measured by [F]fluorodeoxyglucose positron emission tomography is independent of PTEN/AKT status in human colon carcinoma cells. Transl Oncol 2011;4:241–8.
13. Specht JM, Kurland BF, Montgomery SK, Dunnwald LK, Doot RK, Gralow JR, et al. Tumor metabolism and blood flow as assessed by positron emission tomography varies by tumor subtype in locally advanced breast cancer. Clin Cancer Res 2010;16:2803–10.
14. Basu S, Chen W, Tchou J, Mavi A, Cermik T, Czerniecki B, et al. Comparison of triple-negative and estrogen receptor-positive/progesterone receptor-positive/HER2-negative breast carcinoma using quantitative fluorine-18 fluorodeoxyglucose/positron emission tomography imaging parameters: a potentially useful method for disease characterization. Cancer 2008;112:995–1000.
15. Jacobs MA, Ouwerkerk R, Wolff AC, Gabrielson E, Warzecha H, Jeter S, et al. Monitoring of neoadjuvant chemotherapy using multiparametric, (23)Na sodium MR, and multimodality (PET/CT/MRI) imaging in locally advanced breast cancer. Breast Cancer Res Treat 2011;128:119–26.
16. Mankoff DA, Dunnwald LD LK, Doot RK, Specht JM, Gralow JR, Ellis GK, et al. PET tumor metabolism in locally advanced breast cancer

patients undergoing neoadjuvant chemotherapy: value of static versus kinetic measures of fluorodeoxyglucose uptake. Clin Cancer Res 2011;17:2400–9.

17. Minami H, Kawada K, Murakami K, Sato T, Kojima Y, Ebi H, et al. Prospective study of positron emission tomography for evaluation of the activity of lapatinib, a dual inhibitor of the ErbB1 and ErbB2 tyrosine kinases, in patients with advanced tumors. Jpn J Clin Oncol 2007; 37:44–8.

18. Reilly RM, McLarty K, Fasih A, Scollard DA, Done SJ, Vines DC, et al. (18)F-FDG small-animal PET/CT differentiates trastuzumab-responsive from unresponsive human breast cancer xenografts in athymic mice. J Nucl Med 2009;50:1848–56.

19. Chance B, Schoener B, Oshino R, Itshak F, Nakase Y. Oxidation-reduction ratio studies of mitochondria in freeze-trapped samples. NADH and flavoprotein fluorescence signals. J Biol Chem 1979;254: 4764–71.

20. Skala MC, Riching KM, Gendron-Fitzpatrick A, Eickhoff J, Eliceiri KW, White JG, et al. In vivo multiphoton microscopy of NADH and FAD redox states, fluorescence lifetimes, and cellular morphology in precancerous epithelia. Proc Natl Acad Sci U S A 2007;104:19494–9.

21. Walsh AJ, Poole KM, Duvall CL, Skala MC. Ex vivo optical metabolic measurements from cultured tissue reflect in vivo tissue status. J Biomed Opt 2012;17:116015.

22. Lakowicz J. Principles of fluorescence spectroscopy. New York: Plenum Publishers; 1999.

23. Lakowicz JR, Szmacinski H, Nowaczyk K, Johnson ML. Fluorescence lifetime imaging of free and protein-bound Nadh. Proc Natl Acad Sci U S A 1992;89:1271–5.

24. Nakashima N, Yoshihara K, Tanaka F, Yagi K. Picosecond fluorescence lifetime of the coenzyme of D-amino acid oxidase. J Biol Chem 1980;255:5261–3.

25. Maeda-Yorita K, Aki K. Effect of nicotinamide adenine dinucleotide on the oxidation-reduction potentials of lipoamide dehydrogenase from pig heart. J Biochem 1984;96:683–90.

26. Sidani M, Wyckoff J, Xue CS, Segall JE, Condeelis J. Probing the microenvironment of mammary tumors using multiphoton microscopy. J Mammary Gland Biol 2006;11:151–63.

27. Bird DK, Yan L, Vrotsos KM, Eliceiri KW, Vaughan EM, Keely PJ, et al. Metabolic mapping of MCF10A human breast cells via multiphoton fluorescence lifetime imaging of the coenzyme NADH. Cancer Res 2005;65:8766–73.

28. Ritter CA, Perez-Torres M, Rinehart C, Guix M, Dugger T, Engelman JA, et al. Human breast cancer cells selected for resistance to trastuzumab in vivo overexpress epidermal growth factor receptor and ErbB ligands and remain dependent on the ErbB receptor network. Clin Cancer Res 2007;13:4909–19.

29. Miller TW, Forbes JT, Shah C, Wyatt SK, Manning HC, Olivares MG, et al. Inhibition of mammalian target of rapamycin is required for optimal antitumor effect of HER2 inhibitors against HER2-overexpressing cancer cells. Clin Cancer Res 2009;15:7266–76.

30. Gee MS, Upadhyay R, Bergquist H, Alencar H, Reynolds F, Maricevich M, et al. Human breast cancer tumor models: molecular imaging of drug susceptibility and dosing during HER2/neu-targeted therapy. Radiology 2008;248:925–35.

31. Dandekar M, Tseng JR, Gambhir SS. Reproducibility of 18F-FDG microPET studies in mouse tumor xenografts. J Nucl Med 2007;48: 602–7.

32. Fueger BJ, Czernin J, Hildebrandt I, Tran C, Halpern BS, Stout D, et al. Impact of animal handling on the results of 18F-FDG PET studies in mice. J Nucl Med 2006;47:999–1006.

33. McKinley ET, Bugaj JE, Zhao P, Guleryuz S, Mantis C, Gokhale PC, et al. 18FDG-PET predicts pharmacodynamic response to OSI-906, a dual IGF-1R/IR inhibitor, in preclinical mouse models of lung cancer. Clin Cancer Res 2011;17:3332–40.

34. Akaike H. A new look at the statistical model identification. IEEE Transactions on Automatic Control 1974;19:716–23.

35. Huang S, Heikal AA, Webb WW. Two-photon fluorescence spectroscopy and microscopy of NAD(P)H and flavoprotein. Biophys J 2002; 82:2811–25.

36. Yu Q, Heikal AA. Two-photon autofluorescence dynamics imaging reveals sensitivity of intracellular NADH concentration and conformation to cell physiology at the single-cell level. J Photochem Photobiol B 2009;95:46–57.

37. Cheng CM, Cohen M, Wang J, Bondy CA. Estrogen augments glucose transporter and IGF1 expression in primate cerebral cortex. FASEB J 2001;15:907–15.

38. Ostrander JH, McMahon CM, Lem S, Millon SR, Brown JQ, Seewaldt VL, et al. Optical redox ratio differentiates breast cancer cell lines based on estrogen receptor status. Cancer Res 2010;70:4759–66.

39. Chen JQ, Brown TR, Russo J. Regulation of energy metabolism pathways by estrogens and estrogenic chemicals and potential implications in obesity associated with increased exposure to endocrine disruptors. Biochim Biophys Acta 2009;1793:1128–43.

40. Yadav RN. Isocitrate dehydrogenase activity and its regulation by estradiol in tissues of rats of various ages. Cell Biochem Funct 1988; 6:197–202.

41. Pastorelli R, Carpi D, Airoldi L, Chiabrando C, Bagnati R, Fanelli R, et al. Proteome analysis for the identification of in vivo estrogen-regulated proteins in bone. Proteomics 2005;5:4936–45.

42. Narayan M, Wilken JA, Harris LN, Baron AT, Kimbler KD, Maihle NJ. Trastuzumab-induced HER reprogramming in "resistant" breast carcinoma cells. Cancer Res 2009;69:2191–4.

43. Kuznetsov AV, Usson Y, Leverve X, Margreiter R. Subcellular heterogeneity of mitochondrial function and dysfunction: evidence obtained by confocal imaging. Mol Cell Biochem 2004;256–257:359–65.

44. Benard F, Aliaga A, Rousseau JA, Cadorette J, Croteau E, van Lier JE, et al. A small animal positron emission tomography study of the effect of chemotherapy and hormonal therapy on the uptake of 2-deoxy-2-[F-18]fluoro-D-glucose in murine models of breast cancer. Mol Imaging Biol 2007;9:144–50.

45. Drezek R, Brookner C, Pavlova I, Boiko I, Malpica A, Lotan R, et al. Autofluorescence microscopy of fresh cervical-tissue sections reveals alterations in tissue biochemistry with dysplasia. Photochem Photobiol 2001;73:636–41.

46. Skala MC, Fontanella A, Lan L, Izatt JA, Dewhirst MW. Longitudinal optical imaging of tumor metabolism and hemodynamics. J Biomed Opt 2010;15:011112.

47. Suhling K, French PM, Phillips D. Time-resolved fluorescence microscopy. Photochem Photobiol Sci 2005;4:13–22.

48. Kamohara S, Burcelin R, Halaas JL, Friedman JM, Charron MJ. Acute stimulation of glucose metabolism in mice by leptin treatment. Nature 1997;389:374–7.

49. Hundal RS, Petersen KF, Mayerson AB, Randhawa PS, Inzucchi S, Shoelson SE, et al. Mechanism by which high-dose aspirin improves glucose metabolism in type 2 diabetes. J Clin Invest 2002; 109:1321–6.

50. Kantor PF, Lucien A, Kozak R, Lopaschuk GD. The antianginal drug trimetazidine shifts cardiac energy metabolism from fatty acid oxidation to glucose oxidation by inhibiting mitochondrial long-chain 3-ketoacyl coenzyme A thiolase. Circ Res 2000;86:580–8.

Cancer Research

AACR

Quantitative Optical Imaging of Primary Tumor Organoid Metabolism Predicts Drug Response in Breast Cancer

Alex J. Walsh, Rebecca S. Cook, Melinda E. Sanders, et al.

Updated version	Access the most recent version of this article at: doi:10.1158/0008-5472.CAN-14-0663
Supplementary Material	Access the most recent supplemental material at: http://cancerres.aacrjournals.org/content/suppl/2014/08/16/0008-5472.CAN-14-0663.DC1.html

E-mail alerts	Sign up to receive free email-alerts related to this article or journal.
Reprints and Subscriptions	To order reprints of this article or to subscribe to the journal, contact the AACR Publications Department at pubs@aacr.org.
Permissions	To request permission to re-use all or part of this article, contact the AACR Publications Department at permissions@aacr.org.

Quantitative Optical Imaging of Primary Tumor Organoid Metabolism Predicts Drug Response in Breast Cancer

Alex J. Walsh[1], Rebecca S. Cook[2,4], Melinda E. Sanders[4,5], Luigi Aurisicchio[6], Gennaro Ciliberto[7], Carlos L. Arteaga[2,3,4], and Melissa C. Skala[1]

Abstract

There is a need for technologies to predict the efficacy of cancer treatment in individual patients. Here, we show that optical metabolic imaging of organoids derived from primary tumors can predict the therapeutic response of xenografts and measure antitumor drug responses in human tumor–derived organoids. Optical metabolic imaging quantifies the fluorescence intensity and lifetime of NADH and FAD, coenzymes of metabolism. As early as 24 hours after treatment with clinically relevant anticancer drugs, the optical metabolic imaging index of responsive organoids decreased ($P < 0.001$) and was further reduced when effective therapies were combined ($P < 5 \times 10^{-6}$), with no change in drug-resistant organoids. Drug response in xenograft-derived organoids was validated with tumor growth measurements *in vivo* and staining for proliferation and apoptosis. Heterogeneous cellular responses to drug treatment were also resolved in organoids. Optical metabolic imaging shows potential as a high-throughput screen to test the efficacy of a panel of drugs to select optimal drug combinations. *Cancer Res; 74(18); 1–11.* ©2014 AACR.

Introduction

With the ever-increasing number of drugs approved to treat cancers, selection of the optimal treatment regimen for an individual patient is challenging. Physicians weigh the potential benefits of the drugs against the side-effects to the patient. Currently, drug regimens for breast cancer are chosen on the basis of tumor expression of several proteins, including estrogen receptor (ER), progesterone receptor, and high levels of human epidermal growth factor receptor 2 (HER2), assessed in the diagnostic biopsy, and drug effectiveness is determined after weeks of treatment from tumor size measurements. A personalized medicine approach would identify the optimal treatment regimen for an individual patient and reduce morbidity from overtreatment.

Current methods to assess therapy response include tumor size, measured by mammography, MRI, or ultrasound. These methods evaluate the regimen that the patient received.

Molecular changes induced by antitumor drugs precede changes in tumor size and may provide proximal endpoints of drug response. Cellular metabolism may provide biomarkers of early treatment response, because oncogenic drivers typically affect metabolic signaling (1, 2). Indeed fluoro-deoxy-glucose (FDG)–PET has been explored as a predictor of response but lacks the resolution and sensitivity to accurately predict therapy response on a cellular level (3, 4).

Optical metabolic imaging (OMI) provides unique sensitivity to detect metabolic changes that occur with cellular transformation (5–10) and upon treatment with anticancer drugs (11). OMI uses the intrinsic fluorescence properties of NADH and FAD, coenzymes of metabolic reactions. OMI endpoints include the optical redox ratio (the fluorescence intensity of NADH divided by the fluorescence intensity of FAD), the NADH and FAD fluorescence lifetimes, and the "OMI index" (a linear combination of these three endpoints). The optical redox ratio provides a dynamic readout of cellular metabolism (12), with increased redox ratio (NADH/FAD; ref. 8) observed in malignant cells exhibiting the Warburg effect (increased glycolysis despite the presence of oxygen; ref. 13). Fluorescence lifetime values report differences in fluorophore conformation, binding, and microenvironment, such as pH, temperature, and proximity to quenchers such as free oxygen (14). OMI endpoints report early, molecular changes due to anticancer drug treatment (11), and are powerful biomarkers of drug response.

Primary tumors can be cultured *ex vivo* as organoids, which contain the malignant tumor cells and the supporting cells from the tumor environment, such as fibroblasts, leukocytes, endothelial cells, and hematopoietic cells (15). Interactions between cancer cells and stromal cells have been shown to mediate therapeutic resistance in tumors (16). Therefore, organoid cultures provide an attractive platform to test cancer

[1]Department of Biomedical Engineering, Vanderbilt University, Nashville, Tennessee. [2]Department of Cancer Biology, Vanderbilt University, Nashville, Tennessee. [3]Department of Medicine, Vanderbilt University, Nashville, Tennessee. [4]Breast Cancer Research Program, Vanderbilt-Ingram Cancer Center, Vanderbilt University, Nashville, Tennessee. [5]Department of Pathology, Microbiology & Immunology, Vanderbilt University Medical Center, Nashville, Tennessee. [6]Takis Biotech, Rome, Italy. [7]IRCCS National Cancer Institute "G. Pascale," Naples, Italy.

Note: Supplementary data for this article are available at Cancer Research Online (http://cancerres.aacrjournals.org/).

Corresponding Author: Melissa C. Skala, Department of Biomedical Engineering, Vanderbilt University, Station B, Box 351631, Nashville, TN 37235. Phone: 615-322-2602; Fax: 615-343-7919; E-mail: m.skala@vanderbilt.edu

doi: 10.1158/0008-5472.CAN-14-0663

©2014 American Association for Cancer Research.

cell response to drugs in a relevant, "body-like" environment. Furthermore, multiple organoids can be generated from one biopsy, enabling high-throughput tests of multiple drug combinations with a small amount of tissue.

OMI of primary tumor organoids enables high-throughput screening of potential drugs and drug combinations to identify the most effective treatment for an individual patient. Here, we validate OMI in primary tumor organoid cultures as an accurate, early predictor of *in vivo* tumor drug response in mouse xenografts, and present the feasibility of this approach on primary human tissues. The cellular resolution of this technique also allows for subpopulations of cells to be tracked over time with treatment, to identify therapies that affect all cells in a heterogeneous population.

Materials and Methods

Mouse xenografts

This study was approved by the Vanderbilt University Animal Care and Use Committee and meets the NIH guidelines for animal welfare. BT474 cells or HR6 cells (10^8) in 100 μL Matrigel were injected in the inguinal mammary fat pads of female athymic nude mice (J:NU; The Jackson Laboratory). Tumors grew to $\geq$200 mm^3. Tumor-bearing mice were treated twice weekly with the following drugs: control human IgG (10 mg/kg, i.p.; R&D Systems), trastuzumab (10 mg/kg, i.p.; Vanderbilt Pharmacy), paclitaxel (2.5 mg/kg, i.p.; Vanderbilt Pharmacy), XL147 (10 mg/kg, oral gavage; Selleck Chemicals), trastuzumab + XL147, trastuzumab + paclitaxel, and trastuzumab + paclitaxel + XL147. Tumor volume was calculated from caliper measurements of tumor length (L) and width (W), ($L \times W^2$)/2, twice a week.

Primary human tissue collection

This study was approved by the Vanderbilt University Institutional Review Board and informed consent was obtained from all subjects. A primary tumor biopsy, removed from the tumor mass after surgical resection, was provided by an expert breast pathologist (M.E. Sanders). The tumor was placed immediately in sterile DMEM, transported on ice to the laboratory (~5-minute walk), and generated into organoids within 3 hours of tissue resection. Pathology and receptor status of the tissue were obtained from the patient's medical chart.

Organoid generation and culture

Breast tumors (xenografts and primary) were washed three times with PBS. Tumors were mechanically dissociated into 100 to 300 μm macrosuspensions in 0.5 mL primary mammary epithelial cell (PMEC) media [DMEM:F12 + EGF (10 ng/mL) + hydrocortisone (5 μg/mL) + insulin (5 μg/mL) + 1% penicillin:streptomycin] by cutting the tissues with a scalpel or by spinning in a C-tube (Miltenyi Biotec). Macrosuspension solutions were combined with Matrigel in a 1:2 ratio, and 100 μL of the solution was placed on cover slips. The gels solidified at room temperature for 30 minutes and then for 1 hour in the incubator. The gels were over-lain with PMEC media supplemented with drugs. The following *in vitro* drug dosages were used to replicate *in vivo* doses

(17–19): control (control human IgG + DMSO), trastuzumab (25 μg/mL), paclitaxel (0.5 μmol/L), XL147 (25 nmol/L), tamoxifen (2 μmol/L), fulvestrant (1 μmol/L), and A4 (10 μg/mL; Takis Biotech, Inc.).

Fluorescence lifetime instrumentation

Fluorescence lifetime imaging was performed on a custom-built multiphoton microscope (Bruker), as described previously (11, 20). Excitation and emission light were coupled through a 40× oil immersion objective (1.3 NA) within an inverted microscope (Nikon; TiE). A titanium:sapphire laser (Coherent Inc.) was tuned to 750 nm for NADH excitation (average power, 7.5–7.9 mW) and 890 nm for FAD excitation (average power, 8.4–8.6 mW). Bandpass filters, 440/80 nm for NADH and 550/100 nm for FAD, isolated emission light. A pixel dwell time of 4.8 microseconds was used to acquire 256 × 256 pixel images. Each fluorescence lifetime image was collected using time-correlated single-photon counting electronics (SPC-150; Becker and Hickl) and a GaAsP PMT (H7422P-40; Hamamatsu). Photon count rates were maintained above 5 × 10^5 for the entire 60-second image acquisition time, ensuring that no photobleaching occurred. The instrument response full width at half maximum was 260 picoseconds as measured from the second harmonic generation of a urea crystal. Daily fluorescence lifetime validation was confirmed by imaging of a fluorescent bead (Polysciences Inc). The measured lifetime of the bead (2.1 ± 0.06 nanoseconds) concurs with published values (10, 20, 21).

Organoid imaging

Fluorescence lifetime images of organoids were acquired at 24, 48, and 72 hours after drug treatment. Organoids were grown in 35-mm glass-bottom Petri dishes (MatTek Corp) and imaged directly through the coverslip on the bottom of the Petri dish. Six representative organoids from each treatment group were imaged. The six organoids imaged contained collectively approximately 60 to 300 cells per treatment group for statistical and subpopulation analyses. First, an NADH image was acquired and a subsequent FAD image was acquired of the exact same field of view.

Immunofluorescence

A previously reported protocol (22) was adapted for immunofluorescent staining of organoids. Briefly, gels were washed with PBS and fixed with 2 mL 4% paraformaldehyde in PBS. Gels were washed with PBS, and then 0.15 mol/L glycine in PBS was added for 10 minutes. Gels were washed in PBS, and then added to 0.02% Triton X-100 in PBS. Gels were washed with PBS then overlain with 1% fatty acid–free BSA, 1% donkey serum in PBS. The next day, the solution was removed and 100 μL of antibody solution (diluted antibody in PBS with 1% donkey serum) was added to each gel. The gels were incubated for 30 minutes at room temperature, washed in PBS three times, and then incubated in 100 μL of secondary antibody solution for 30 minutes at room temperature. The gels were washed in PBS three times, washed in water twice, and then mounted on slides using 30 μL of the ProLong Antifade Solution (Molecular Probes).

The primary antibodies used were anti-cleaved caspase-3 (Life Technologies) and anti-Ki67 (Life Technologies). Both were diluted at 1:100. A goat anti-rabbit IgG FITC secondary antibody was used (Life Technologies). FITC fluorescence was obtained by excitation at 980 nm on the multiphoton microscope described above, and a minimum of six organoids were imaged. Positive staining of cleaved caspase-3 and Ki67 was confirmed by staining mouse thymus and mouse small intestine, respectively. Immunofluorescence images were quantified by manual counting of the total number of cells and the number of positively stained cells in each field of view. Immunofluorescence results were presented as percentage of positively stained cells, quantified from six organoids, approximately 200 cells.

Generation of OMI endpoint images

Photon counts for nine surrounding pixels were binned (SPCImage). Fluorescence lifetime components were extracted from the photon decay curves by deconvolving the measured system response and fitting the decay to a two-component model, $I(t) = \alpha_1 \exp^{-t/\tau_1} + \alpha_2 \exp^{-t/\tau_2} + C$, where $I(t)$ is the fluorescence intensity at time t after the laser pulse, α_1 and α_2 are the fractional contributions of the short and long lifetime components, (i.e., $\alpha_1 + \alpha_2 = 1$), τ_1 and τ_2 are the fluorescence lifetimes of the short and long lifetime components, and C accounts for background light. A two-component decay was used to represent the lifetimes of the free and bound configurations of NADH and FAD (10, 23, 24) and yielded the lowest χ^2 values (0.99–1.1), indicative of an optimal fit. Matrices of the lifetime components were exported as ascii files for further processing in Matlab.

Automated image analysis software

To streamline the cellular-level processing of organoid images, an automated image analysis routine, as previously described (25), was used in Cell Profiler in Matlab. Briefly, a customized threshold code identified pixels belonging to nuclear regions that were brighter than background but not as bright as cell cytoplasms. These nuclear pixels were smoothed and the resulting round objects between 6 and 25 pixels in diameter were segmented and saved as the nuclei within the image. Cells were identified by propagating out from the nuclei. An Otsu Global threshold was used to improve propagation and prevent propagation into background pixels. Cell cytoplasms were defined as the cells minus the nuclei. Cytoplasm values were measured from each OMI image (redox ratio, NADH τ_m, NADH τ_1, NADH τ_2, NADH α_1, FAD τ_m, FAD τ_1, FAD τ_2, and FAD α_1).

Computation of OMI index

The redox ratio, NADH τ_m, and FAD τ_m were norm-centered across cell values from all treatment groups within a sample, resulting in unitless parameters with a mean of 1. The OMI index is the linear combination of the norm-centered redox ratio, NADH τ_m, and FAD τ_m, with the coefficients (1, 1, and −1), respectively, computed for each cell. The three endpoints, redox ratio, NADH τ_m, and FAD τ_m are independent variables (11) and are thus weighted equally. The signs of the coefficients were chosen to maximize difference between control and drug-responding cells.

Subpopulation analysis

Subpopulation analysis was performed by generating histograms of all cell values within a group as previously reported (11). Each histogram was fit to 1, 2, and 3 component Gaussian curves. The lowest Akaike information criterion (AIC) signified the best fitting probability density function for the histogram (26). Probability density functions were normalized to have an area under the curve equal to 1.

Statistical tests

Differences in OMI endpoints between treatment groups were tested using a student t test with a Bonferroni correction. An α significance level less than 0.05 was used for all statistical tests.

Results

Response of BT474 organoids to a panel of anticancer drugs

Validation of an organoid-OMI screen for drug response was first tested in two isogenic HER2-amplified breast cancer xenografts. BT474 xenografts are sensitive to the HER2 antibody trastuzumab, whereas HR6 xenografts, derived as a subline of BT474, are trastuzumab resistant. The following single drugs and drug combinations were tested: paclitaxel (P; chemotherapy), trastuzumab (H; anti-HER2 antibody), XL147 (X; PI3K small-molecule inhibitor; ref. 27), H+P, H+X, and H+P+X. Paclitaxel and trastuzumab are standard-of-care drugs, and XL147 is in clinical trials and preclinical studies support combination therapy of XL147 with trastuzumab for patients who have developed a resistance to trastuzumab (27, 28).

Representative redox ratio, NADH τ_m, and FAD τ_m images of BT474 xenograft-derived organoids demonstrate mixed multicellular morphology and highlight the subcellular resolution of this technique (Fig. 1A–F). A longitudinal study of tumor growth demonstrated that the BT474 xenografts responded to each treatment arm (Fig. 1G), with significant reduction in tumor volume, as determined from caliper measurements, on day 7 for all treatment groups except trastuzumab, which had significant reduction on day 11 (Fig. 1H).

A composite endpoint, the OMI index, was computed as a linear combination of the mean-normalized optical redox ratio, NADH τ_m, and FAD τ_m for each cell. After 24 hours of treatment, the OMI index was significantly reduced in all treated BT474 organoids, compared with the control ($P < 0.05$; Fig. 1I). By 72 hours, the OMI index decreased further in all the treatment groups ($P < 5 \times 10^{-7}$, Fig. 1J). The redox ratio, NADH τ_m, and FAD τ_m values showed similar trends (Supplementary Fig. S1). Changes in short and long lifetime values and in the portion of free NADH or FAD contributed to the changes in τ_m (Supplementary Table S1).

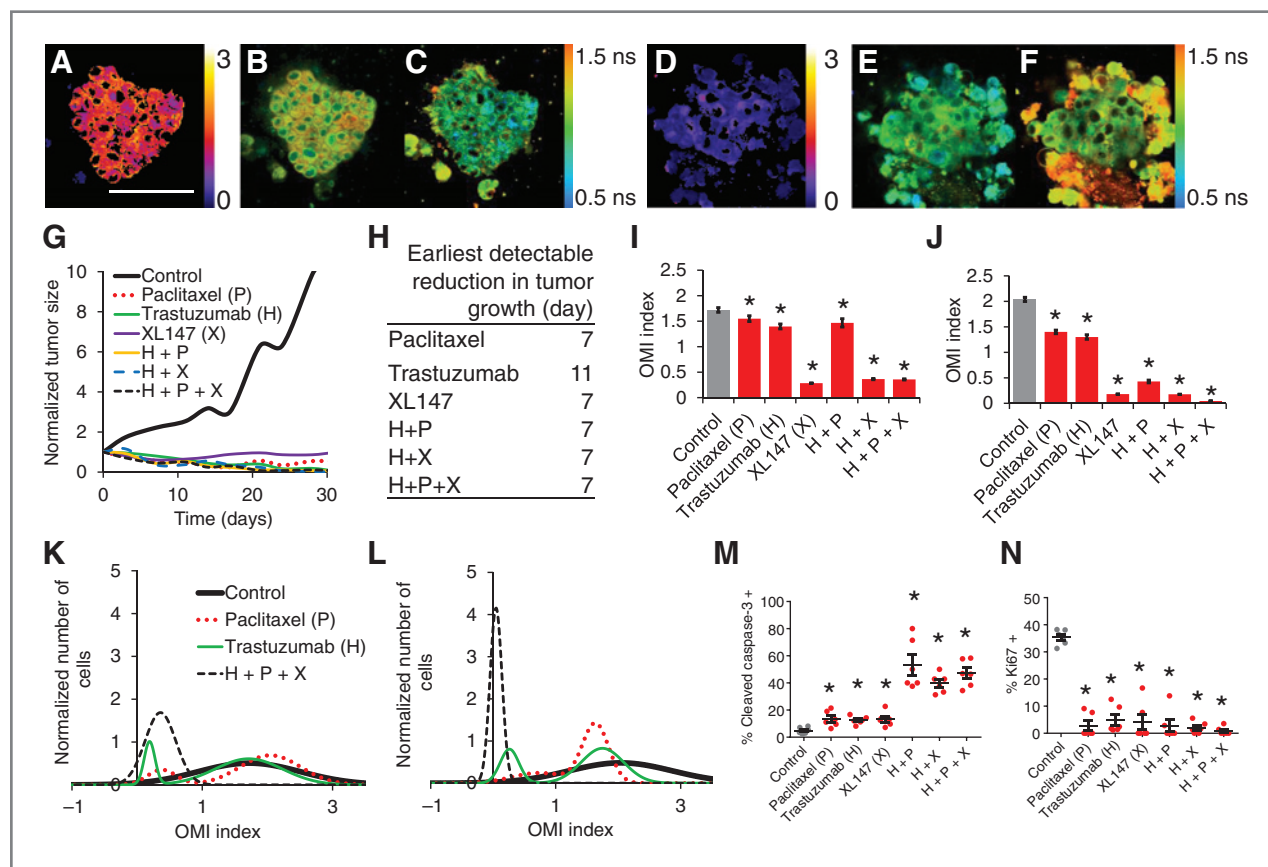The high-resolution capabilities of OMI allowed single-cell analysis and population modeling for quantification of

Figure 1. OMI of organoids derived from trastuzumab-responsive xenografts. A, redox ratio image of a control BT474 (ER$^+$/HER2$^+$) organoid at 72 hours. Scale bar, 100 μm. B, NADH τ_m image of a control BT474 organoid at 72 hours. C, FAD τ_m image of a control BT474 organoid at 72 hours. D, redox ratio image of a trastuzumab (anti-HER2) plus paclitaxel (chemotherapy) plus XL147 (anti-PI3K; H+P+X)–treated BT474 organoid at 72 hours. E, NADH τ_m image of a trastuzumab plus paclitaxel plus XL147 (H+P+X)–treated BT474 organoid at 72 hours. F, FAD τ_m image of a trastuzumab plus paclitaxel plus XL147 (H+P+X)–treated BT474 organoid at 72 hours. G, tumor growth response of BT474 tumors grown in athymic nude mice and treated with single and combination treatments. H, table of earliest detectable ($P < 0.05$) reduction in tumor size for control versus treated mice. I, OMI index decreases in BT474 organoids treated with single and combination therapies at 24 hours. J, OMI index of BT474 organoids treated for 72 hours. Red bars, $P < 0.05$ for treated organoids versus control. K, population density modeling of the mean OMI index per cell in control, paclitaxel, trastuzumab, and H+P+X–treated organoids at 24 hours. L, population density modeling of the OMI index for control, paclitaxel, trastuzumab, and H+P+X BT474 organoids treated for 72 hours. M, immunofluorescence staining of cleaved caspase-3 in control and treated BT474 organoids at 72 hours. N, immunofluorescence staining of Ki67 in control and treated BT474 organoids at 72 hours. *, $P < 0.05$.

cellular subpopulations with varying OMI indices. Visual inspection of cell morphology suggested that the majority of cells are tumor epithelial cells; stromal cells with obvious morphologic differences were eliminated from the analysis. Population density modeling of cellular distributions of the OMI index revealed two populations with high and low OMI index values in all of the BT474-treated organoids at 24 hours (Fig. 1K and Supplementary Fig. S2). By 72 hours, the XL147-, H+P-, H+X-, and H+P+X-treated organoids have a single population with narrower peaks (Fig. 1L and Supplementary Fig. S2). The trastuzumab-treated organoids have two populations at 72 hours, both lower than the mean OMI index of the control organoids (Fig. 1L). Immunofluorescent staining of cleaved caspase-3 and Ki67 of BT474 organoids treated for 72 hours confirmed increased apoptosis and decreased proliferation in drug-treated organoids, with the greatest increases in cell death with combined treatments (Fig. 1M and N).

Response of HR6 organoids to a panel of anticancer drugs

Next, the OMI-organoid screen was tested on trastuzumab-resistant HR6 xenografts (29). Representative images show HR6 organoid morphology and spatial distributions of OMI endpoints (Fig. 2A–F). These HER2-overexpressing tumors had continued growth with trastuzumab treatment (Fig. 2G). Treatment with paclitaxel and XL147 initially caused HR6 tumor regression ($P < 0.05$ on day 10 for XL147 and on day 14 for paclitaxel) but then resumed growth (Fig. 2G and H). Mice treated with the H+P, H+X, and H+P+X combination therapies exhibited sustained HR6 tumor reduction (Fig. 2G and H).

After 24 hours of treatment, significant reductions in the OMI index were detected in HR6 organoids treated with paclitaxel, XL147, H+P, H+X, and H+P+X ($P < 0.05$; Fig. 2I). At 72 hours, the OMI index of the paclitaxel- and XL147-treated organoids was significantly greater than that of the
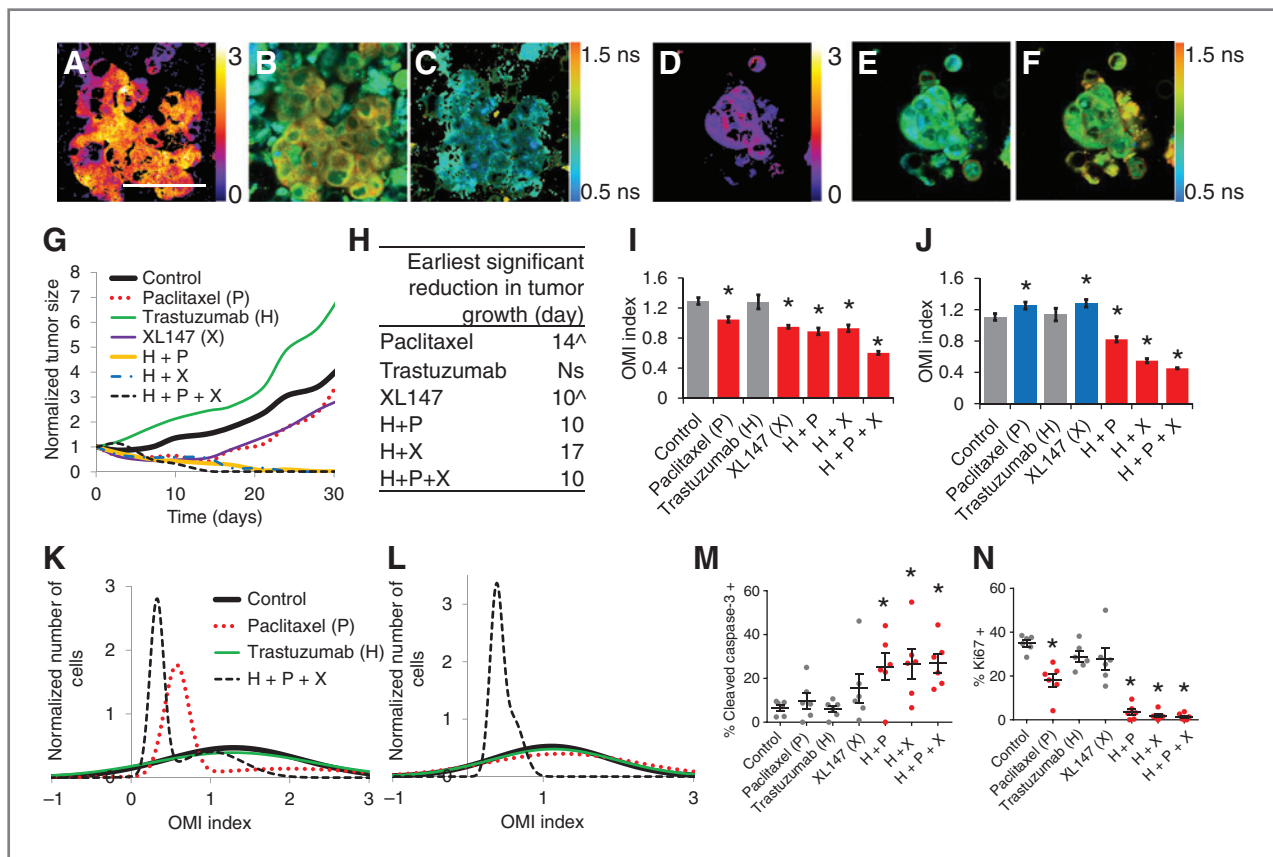
Figure 2. OMI of organoids derived from trastuzumab-resistant xenografts. A, redox ratio image of a control HR6 (ER$^+$/HER2$^+$) organoid at 72 hours. Scale bar, 100 μm. B, NADH τ_m image of a control HR6 organoid at 72 hours. C, FAD τ_m image of a control HR6 organoid at 72 hours. D, redox ratio image of a trastuzumab (anti-HER2) plus paclitaxel (chemotherapy) plus XL147 (anti-PI3K; H+P+X)–treated HR6 organoid at 72 hours. E, NADH τ_m image of an H+P+X-treated HR6 organoid at 72 hours. F, FAD τ_m image of an H+P+X-treated HR6 organoid at 72 hours. G, tumor growth response of HR6 tumors grown in athymic nude mice and treated with single and combination treatments. H, table of earliest detectable ($P < 0.05$) reduction in tumor size for control versus treated mice. ^, tumors that initially shrank and then grew; NS, not significant. I, OMI index initially decreases in HR6 organoids treated with paclitaxel, XL147, and combination therapies at 24 hours. J, OMI index of HR6 organoids treated for 72 hours. Red bars, significant reductions in OMI index; $P < 0.05$, for treated organoids versus control. Blue bars, significant increases in OMI index; $P < 0.05$, for treated organoids versus control. K, population density modeling of the mean OMI index per cell in control, paclitaxel, trastuzumab, and H+P+X organoids at 24 hours. L, population density modeling of the OMI index for HR6 control, paclitaxel, trastuzumab, and H+P+X organoids treated for 72 hours. M, immunofluorescence staining of cleaved caspase-3 in control and treated HR6 organoids at 72 hours. N, immunofluorescence staining of Ki67 in control and treated HR6 organoids at 72 hours. *, $P < 0.05$.

control organoids ($P < 0.05$; ref. Fig. 2J), consistent with the recovery of HR6 tumor growth after prolonged therapy (Fig. 2G). The organoids treated with drug combinations (H+P, H+X, and H+P+X) continued to have significantly lower OMI index values ($P < 10^{-6}$) at 72 hours, compared with untreated controls. Individual OMI endpoints showed similar trends (Supplementary Fig. S3 and Supplementary Table S2). Subpopulation analysis revealed two subpopulations in the OMI index for all treated groups except for trastuzumab at 24 hours (Fig. 2K and Supplementary Fig. S4). By 72 hours, the paclitaxel- and XL147-treated organoids had a single population (Fig. 2L and Supplementary Fig. S4). Immunofluorescent staining of cleaved caspase-3 of organoids treated for 72 hours revealed increased cell death in HR6 organoids treated with H+P, H+X, and H+P+X ($P < 0.05$, Fig. 2M). The percentage of Ki67-positive cells at 72 hours decreased with paclitaxel, H+P, H+X, and H+P+X treatment ($P < 0.005$, Fig. 2N).

OMI endpoints identify breast cancer subtypes

We tested these methods on primary breast cancer biopsies obtained from surgical resection. Tumors were obtained fresh from deidentified mastectomy specimens not required for further diagnostic purposes, and dissociated into organoids within 1 to 3 hours postresection. Cancer drugs were added and organoids were imaged with OMI. Representative redox ratio, NADH τ_m, and FAD τ_m images (Fig. 3) demonstrate the varying morphology of organoids derived from ER$^+$, HER2$^+$, and triple-negative breast cancers (TNBC).

When quantified, the OMI endpoints differed between cancer subtypes. In immortalized cell lines, the redox ratio was elevated in ER$^+$/HER2$^-$ cells and was greatest in HER2$^+$ cells ($P < 5 \times 10^{-5}$, Fig. 4A). Similarly, NADH τ_m was increased in immortalized ER$^+$/HER2$^-$ and HER2$^+$ breast cancer cells as compared with TNBC cells ($P < 5 \times 10^{-8}$, Fig. 4B). FAD τ_m was greatest in ER$^+$/HER2$^-$ cells ($P < 0.05$, Fig. 4C). Overall, the OMI index was lowest in TNBC and greatest in HER2$^+$
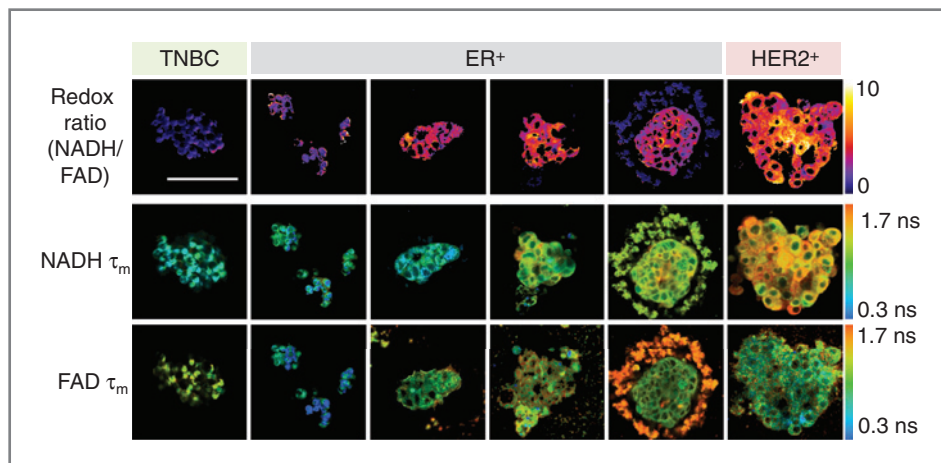
Figure 3. Representative redox ratio, NADH τ_m, and FAD τ_m images of organoids derived from primary, human breast tumors. Redox ratio (NADH/FAD; first row), NADH τ_m (second row), and FAD τ_m (third row) images of organoids generated from primary human breast tissue obtained from resection surgeries. Scale bar, 100 μm.

cells ($P < 5 \times 10^{-8}$, Fig. 4D), suggesting that HER2 and ER expression influence cellular metabolism.

Similar trends were observed for the OMI endpoints in organoids derived from primary breast tumor specimens cultured under basal conditions. The redox ratio was increased in organoids from $ER^+/HER2^-$ tumors and was greatest in $HER2^+/ER^-$ organoids ($P < 5 \times 10^{-12}$; Fig. 4E; Supplementary Table S3). Likewise, NADH τ_m increased with ER and HER2 expression ($P < 5 \times 10^{-8}$; Fig. 4F). FAD τ_m was increased in ER^+ organoids and reduced in $HER2^+$ organoids ($P < 0.05$, Fig. 4G). The OMI index was lowest for TNBC, and greatest for $HER2^+$ organoids ($P < 5 \times 10^{-3}$; Fig. 4H).

Organoid response of ER^+ primary human tumors

Organoids were generated from four ER+ ($HER2^-$) primary human tumors and treated with the chemotherapeutic drug paclitaxel, the selective ER modulator tamoxifen, the HER2 antibody trastuzumab, and the pan-PI3K inhibitor XL147. Organoids derived from the first ER^+ tumor had significantly reduced OMI index values upon treatment with paclitaxel, tamoxifen, XL147, H+X, H+P+T, H+P+X, and H+P+T+X for 72 hours ($P < 5 \times 10^{-5}$, Fig. 5A). Immunofluorescence of cleaved caspase-3 showed increased cell death in parallel organoids treated for 72 hours with paclitaxel, tamoxifen, XL147, H+X, H+P+T, H+P+X, and H+P+T+X (Fig. 5B).
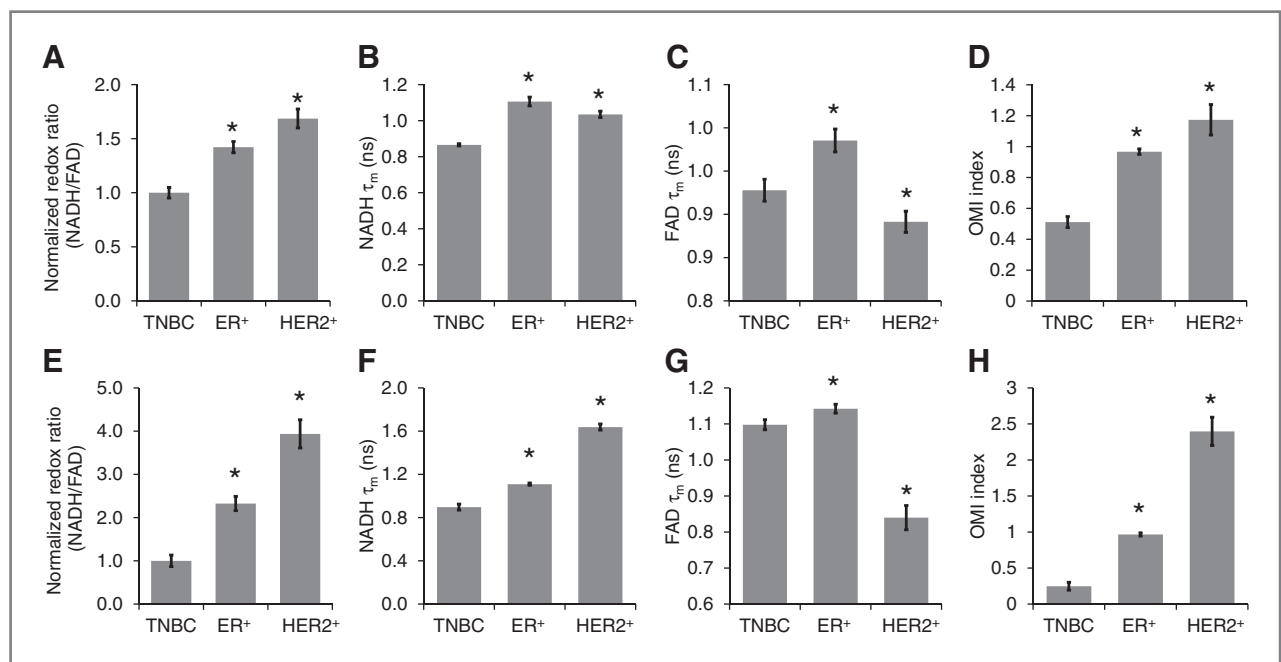

Figure 4. OMI endpoints differ among breast cancer subtypes. A, redox ratio (NADH/FAD) of TNBC cells (MDA-MB-231), ER^+ ($HER2^-$) cells (MCF7), and $HER2^+$ cells (SKBr3, BT474, and MDA-MB-361). B, NADH τ_m of TNBC, ER^+, and $HER2^+$ immortalized cell lines. C, FAD τ_m of TNBC, ER^+, and $HER2^+$ immortalized cell lines. D, OMI index increases in ER^+ and $HER2^+$ immortalized cell lines. E, redox ratio (NADH/FAD) of organoids derived from triple-negative, ER^+ ($HER2^-$), and $HER2^+$ (ER^-) primary human tumors. F, NADH τ_m of organoids derived from triple-negative, ER^+, and $HER2^+$ primary human tumors. G, FAD τ_m of organoids derived from triple-negative, ER^+, and $HER2^+$ primary human tumors. H, OMI index of organoids derived from triple-negative, ER^+, and $HER2^+$ primary human tumors. *, $P < 0.05$.
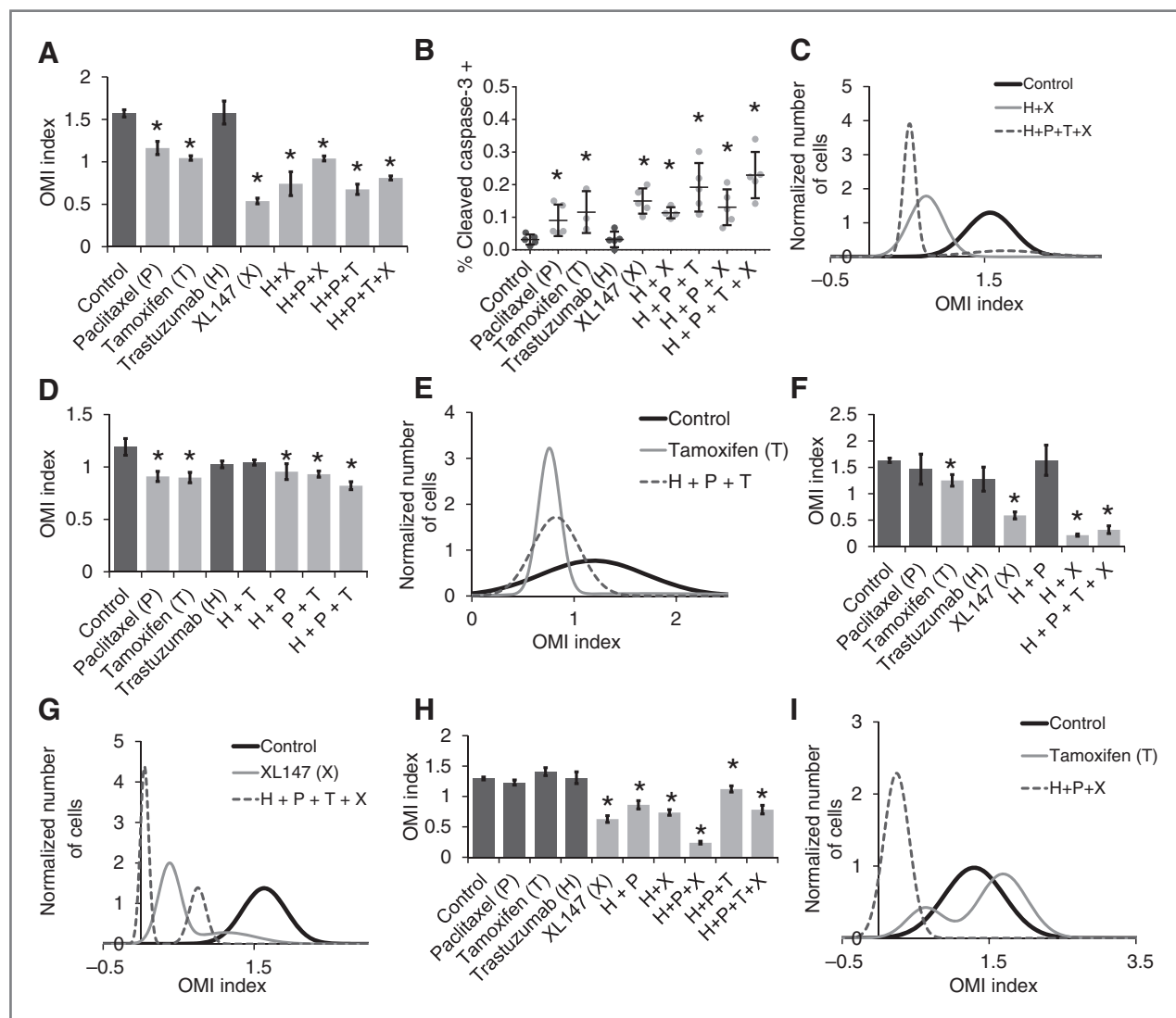
Figure 5. OMI index measures drug response and heterogeneous populations in ER+ primary human tumor–derived organoids. A, OMI index of organoids derived from an ER+ (HER2−) primary human tumor decreased with paclitaxel (chemotherapy), tamoxifen (ER antagonist), XL147 (anti-PI3K), and combined therapies at 72 hours. Light gray bars, significant ($P < 0.05$) reductions in OMI index with treatment versus control organoids. B, quantification of immunofluorescence staining of cleaved caspase-3 for organoids derived from the same tumor sample as in A and treated for 72 hours. C, population density modeling of the control, H+X-, and H+P+T+X-treated organoids presented in A. D, OMI index is reduced with paclitaxel, tamoxifen, and combined treatments in organoids derived from a different ER+ patient at 72 hours. E, population density modeling of the control, tamoxifen, and H+P+T-treated organoids presented in D. F, OMI index is reduced in organoids from a third ER+ patient treated with tamoxifen, XL147, H+X, and H+P+T+X at 24 hours. G, population density modeling of the control, XL147-, and H+P+T+X-treated organoids presented in F. H, organoids derived from a fourth ER+ patient had significant reductions in OMI index when treated with XL147 and combination therapies at 72 hours. I, population density modeling of the control, tamoxifen-, and H+P+X-treated organoids in H revealed multiple populations with tamoxifen treatment. *, $P < 0.05$.

Subpopulation analysis revealed less variability (narrower histogram peaks) within responsive treatment groups compared with the cells of control and trastuzumab-treated organoids (Fig. 5C and Supplementary Fig. S5). Corresponding OMI endpoints showed similar trends (Supplementary Fig. S6 and Supplementary Table S4).

Organoids derived from a second ER+ tumor responded similarly. The OMI index decreased upon treatment with paclitaxel, tamoxifen, H+P, P+T, and H+P+T at 72 hours ($P < 5 \times 10^{-5}$, Fig. 5D). Subpopulation analysis revealed a single

population of control cells that shifted to lower OMI indexes with paclitaxel, tamoxifen, H+P, P+T, and H+P+T treatments (Fig. 5E and Supplementary Fig. S7). Corresponding OMI endpoints showed similar trends (Supplementary Fig. S8 and Supplementary Table S5).

The third and fourth ER+ clinical samples yielded organoids with variable responses to treatment. Organoids derived from the third patient had significant reductions in OMI index after 24 hours of treatment with tamoxifen, XL147, H+X, and H+P+T+X ($P < 0.005$, Fig. 5F). Subpopulation analysis

revealed two populations with high and low OMI index values for the H+P- and paclitaxel-treated organoids (Fig. 5G and Supplementary Fig. S9). Two populations, both with mean OMI index values less than that of the control organoids, were apparent in the organoids treated with XL147 and with H+P+T+X (Fig. 5G and Supplementary Fig. S9). Organoids from the fourth ER$^+$ patient had reduced OMI indices following treatment with XL147, H+P, H+X, H+P+X, H+P+T, and H+P+T+X for 72 hours ($P < 0.01$, Fig. 5H). Subpopulation analysis of cells from these organoids revealed single populations with shifted mean OMI indices for all treatments except tamoxifen, H+P, and H+X, which had two populations (Fig. 5I and Supplementary Fig. S10). Corresponding OMI endpoints showed similar trends (Supplementary Figs. S11–S12 and Supplementary Tables S6–S7).

Organoid Response of HER$^+$ and TNBC primary human tumors

OMI was also performed on organoids derived from HER2$^+$ (ER$^-$) and TNBC specimens. Organoids derived from the HER2$^+$ primary tumor were treated with the ER downregulator fulvestrant, the HER2 antibody trastuzumab, and the anti-ErbB3 antibody A4 (30). The OMI index was significantly decreased in the organoids treated for 24 hours with trastuzumab and A4 ($P < 0.005$, Fig. 6A). Subpopulation analysis revealed shifts in the mean OMI index values with these treatments within a single population of cells (Fig. 6B). Organoids derived from the TNBC specimen were treated with tamoxifen, the HER2 antibody trastuzumab, and the combination of trastuzumab plus tamoxifen (H+T). No significant changes were observed with these treatments in TNBC organoids after 24 hours ($P > 0.3$, Fig. 6C). Subpopulation analysis

revealed a single population of cells from TNBC organoids (Fig. 6D). Corresponding OMI endpoints showed similar trends (Supplementary Figs. S7 and S8 and Supplementary Tables S8 and S9).

Discussion

Primary tumor organoids are an attractive platform for drug screening because they are grown from intact biopsies, thus maintaining the tumor cells within the same tumor microenvironment (15). OMI is sensitive to early metabolic changes, achieves high resolution to allow analysis of tumor cell heterogeneity, and uses endogenous contrast in living cells for repeated measurements and longitudinal studies (11). The OMI index is a holistic reporter of cellular metabolism because the redox ratio and NADH and FAD lifetimes are independent measurements (11). The mean lifetime captures not only changes in free-to-bound protein ratios but also preferred protein binding and relative concentrations of NADH to NADPH (31). Cancer drugs have been shown to downregulate certain metabolism enzymes; for example, trastuzumab downregulates lactate dehydrogenase in breast cancer, and paclitaxel-resistant cells have been shown to have more lactate dehydrogenase expression and activity (32). The OMI index captures these drug-induced changes in metabolism enzyme activity. Organoids remain viable with stable OMI endpoints in controlled culture conditions (33), thus making them an attractive system to evaluate tumor response to drugs. We used OMI to assess the response of primary breast tumor organoids to a panel of clinically relevant anticancer agents used singly or in combination. Early OMI-measured response in organoids (24–72 hours after treatment) corroborated with
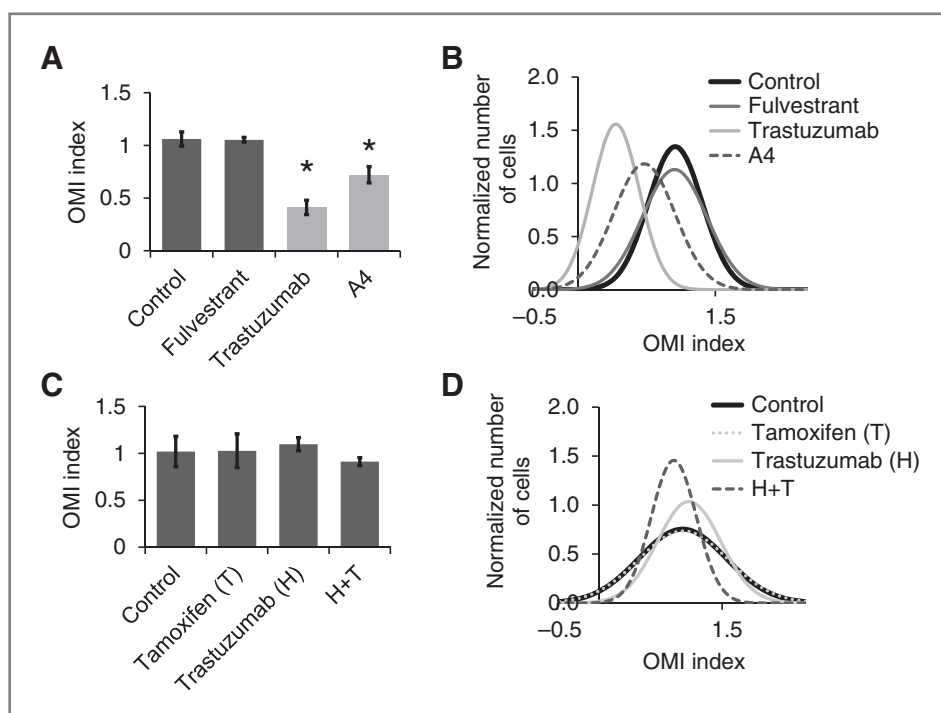

Figure 6. OMI index detects response of HER2$^+$ organoids to trastuzumab and resolves no response in TNBC. A, organoids derived from a HER2$^+$ (ER$^-$) clinical tumor had reduced OMI indices with trastuzumab (anti-HER2) and A4 (anti-ErbB3) treatment, and no change with fulvestrant treatment (ER antagonist) at 24 hours. Light gray bars, significant reductions in OMI index due to drug treatment compared with control organoids ($*$, $P < 0.05$). B, population density modeling of the organoids derived from a HER2$^+$ tumor revealed single populations. C, organoids derived from a TNBC tumor had no significant changes ($P > 0.3$) in OMI index with treatment of targeted therapies, tamoxifen (ER antagonist), and trastuzumab at 48 hours. D, population density modeling revealed single populations within the TNBC organoids.

standard tumor growth curves in xenografts, and the feasibility of this approach was confirmed in organoids derived from primary human breast tumors.

The OMI index was first evaluated as a reporter of tumor response in organoids derived from BT474 (ER$^+$/HER2$^+$) xenografts. Significant reductions in OMI index upon treatment with paclitaxel, trastuzumab, XL147, and combinations thereof, at both 24 and 72 hours, correlated with reduction of tumor growth (Fig. 1). Biochemically, cellular rates of glycolysis, and NADH and FAD protein-binding decrease with drug treatment in responsive cells (32), resulting in decreased redox ratios and NADH τ_m, and increased FAD τ_m in agreement with the decreased OMI index observed in drug-treated BT474 organoids. Significant reductions in tumor growth occurred 7 to 11 days after treatment initiation, whereas the OMI index detected response 24 to 72 hours after treatment. Cellular analysis revealed an initial heterogeneous response among cells within organoids treated with paclitaxel and H+P at 24 hours, which, by 72 hours, became a uniform response. The heterogeneity of trastuzumab-treated BT474 organoids persisted over 72 hours, suggesting an intrinsic subpopulation more susceptible to acquire drug resistance. This heterogeneity was not seen in the combination treatments, suggesting the combination treatments trump this drug resistance–prone subpopulation. OMI-measured response corroborated with increased cell death and decreased proliferation due to single and combination drug–treated organoids, measured with destructive postmortem techniques. The XL147-treated BT474 organoids have a much lower OMI index at 72 hours, but only a modest increase in cleaved caspase-3 activity. The same decrease was not observed in the HR6 cells that have alternative metabolism pathways activated because of their acquired resistance to trastuzumab. The OMI index detects changes in cellular metabolism that predict drug efficacy, but do not necessarily correlate with IHC.

In the current standard of care, patients with innate drug resistance are not identified *a priori*. We tested the capabilities of OMI to predict drug resistance using trastuzumab-resistant HR6 (ER$^+$/HER2$^+$) tumors (29). XL147 is a novel PI3K inhibitor under investigation for combined therapy with trastuzumab to improve response of resistant tumors (27). Significant reductions in the OMI index of HR6 organoids treated for 72 hours identified drug combinations (H+X, H+P, and H+P+X) that induced a sustained reduction in tumor growth *in vivo* (Fig. 2). The reduction in tumor growth upon treatment with H+X was consistent with previous reports of greater antitumor effects of the combination over trastuzumab and XL147 alone (27). Subpopulation analysis revealed multiple responses within the HR6 organoids after treatment with single drugs and combinations, suggesting increased heterogeneity compared with the parental BT474 organoids.

The OMI index of paclitaxel- and XL147-treated HR6 organoids initially decreased at 24 hours, and then increased at 72 hours, mirroring the tumor growth in mice after prolonged therapy, and indicating that the adaptations that allow HR6 cells to survive trastuzumab treatment also affect response to additional drugs. This relapse of HR6 tumors treated with paclitaxel and XL147 was not apparent until 2 to 3 weeks of

drug treatment; yet, the OMI index identified a resistant population within both paclitaxel- and XL147-treated organoids at 24 hours and showed a selection of this population by 72 hours. Subpopulation analysis of the paclitaxel- and XL147-treated HR6 organoids revealed heterogeneous responses at 24 hours, suggesting that OMI is capable of early detection of resistant cells within a heterogeneous tumor. These results indicate that OMI of primary tumor organoids is able to identify heterogeneous responses within tumors on a cellular level, and potentially guide therapy selection early for maximal response. The ability to detect innate resistance at a cellular level before treatment may provide leads for identification of drugs that target such refractory subpopulations before they are selected by the primary therapy.

We next examined the feasibility of this approach using fresh tumor biopsies obtained from primary tumor surgical resections. OMI measurements *in vivo* and corresponding measurements from freshly excised tissues within 8 hours of surgery are statistically identical (20), providing ample time for specimen acquisition and transport to the laboratory. The morphology of organoids differed among patients and within breast cancer subtypes (Fig. 3), demonstrating a greater heterogeneity within primary tumors compared with xenografts.

Previously published studies report differences in OMI endpoints due to the presence or absence of ER and HER2 (8, 11, 34). Both ER and HER2 signaling pathways can influence metabolism: ER by inducing increased glucose transport (1), and HER2 through activation of PI3K (2), among other signal transducers. We compared OMI endpoints from immortalized cells and human tissue-derived organoids of three subtypes of breast cancer: ER$^+$, HER2-overexpressing, and TNBC. The OMI index of immortalized cell lines increased with ER expression and was highest in HER2 overexpressing cells (consistent with prior studies (11)), and these trends were replicated in organoids derived from primary human tumors. Notably, NADH τ_m was significantly increased ($P <$ 0.05) in the HER2$^+$ organoids compared with ER$^+$ organoids, but this trend was not observed in the immortalized cell lines. This difference could be due to molecular changes induced by the immortalization process, media components, primary tumor heterogeneity, and/or the heterogeneity within a primary breast tumor. Regardless, the results shown (Fig. 4) suggest breast cancer subtypes, ER$^+$, HER2$^+$ and TNBC, have different OMI profiles.

Organoids derived from human breast tumors were treated with a panel of breast cancer drugs (Figs. 5 and 6). Differences in the drug response of these organoids suggest heterogeneity across ER$^+$/HER$^-$ tumors. Organoids from one of the four ER$^+$ tumors did not exhibit reduced OMI indices after treatment with tamoxifen. Organoids derived from two of the four ER$^+$ samples did not have reduced OMI indices after paclitaxel treatment. These variable responses are consistent with variable responses seen with these drugs in the clinic (35–38). None of the organoids had reduced OMI indices with trastuzumab, which is expected because the organoids were derived from HER2$^-$ tumors. Generally, the OMI index was reduced further upon treatment with drug combinations, supporting the use of drug combinations clinically.

Subpopulation analysis revealed cells within organoid treatment groups that exhibit different OMI indices after treatment, suggesting that subpopulations of cells with different drug sensitivities preexist and develop within primary tumors. Some of these cells may represent the cancer stem-like population with increased renewal capacity, metastatic potential, and drug resistance (39). The populations of organoids derived from human tumors have more variability (broader population curves) than those derived from xenografts, reflecting an inherent greater heterogeneity within primary tumors. This corroborates previous reports (40) of greater intratumoral heterogeneity in primary tumors than in xenografts derived from clonal cell lines. Thus, OMI imaging allows identification of heterogeneous cellular response to drug treatment in a dynamic population, which potentially enables drug selection to maximize therapeutic efficacy.

Organoids derived from $HER2^+/ER^-$ and TNBC primary tumors have OMI responses consistent with their clinical characteristics: reduced OMI index with trastuzumab treatment and no change with fulvestrant (ER antagonist) treatment in the $HER2^+/ER^-$ organoids (41), and no OMI index reductions after treatment with trastuzumab or tamoxifen in the TNBC organoids (Fig. 6a and c; refs. 42, 43). HER3 is an emerging target for breast cancer (30, 44) and the anti-HER3 antibody A4 reduced the OMI index of $HER2^+/ER^-$ organoids.

The results of this study support the validity of OMI for monitoring organoid response to anticancer drugs. We demonstrate high selectivity of the OMI index to directly measure drug response of organoids derived from breast cancer xenografts to single anticancer drugs and their combinations, and validated OMI measured response with gold standard tumor growth in two xenograft models. We have shown that the OMI index measured in primary tumor organoids resolves response and nonresponse within 72 hours, compared with the 3 weeks required to resolve this response with tumor size measurements. Furthermore, we extend this approach and generate drug response information from organoids derived from three subtypes of primary human tumors, TNBC, ER^+, and $HER2^+$. The high resolution of OMI allows subpopulation analysis for identification of heterogeneous tumor response to drugs in dynamic tumor cell populations. Altogether, these results suggest that OMI of primary tumor organoids may be a powerful test to predict the action of anticancer drugs and tailor treatment decisions accordingly.

Disclosure of Potential Conflicts of Interest

L. Aurisicchio has ownership interest (including patents) in Takis Biotech. No potential conflicts of interest were disclosed by the other authors.

Authors' Contributions

Conception and design: A.J. Walsh, M.E. Sanders, M.C. Skala
Development of methodology: A.J. Walsh, M.C. Skala
Acquisition of data (provided animals, acquired and managed patients, provided facilities, etc.): A.J. Walsh, R.S. Cook, M.E. Sanders, C.L. Arteaga, M.C. Skala
Analysis and interpretation of data (e.g., statistical analysis, biostatistics, computational analysis): A.J. Walsh, R.S. Cook, M.E. Sanders, M.C. Skala
Writing, review, and/or revision of the manuscript: A.J. Walsh, R.S. Cook, M.E. Sanders, L. Aurisicchio, G. Ciliberto, C.L. Arteaga, M.C. Skala
Administrative, technical, or material support (i.e., reporting or organizing data, constructing databases): C.L. Arteaga
Study supervision: M.C. Skala
Other (providing some key reagents): L. Aurisicchio
Other (providing monoclonal antibodies used for a subset of experiments reported in the article): G. Ciliberto

References

1. Cheng CM, Cohen M, Wang J, Bondy CA. Estrogen augments glucose transporter and IGF1 expression in primate cerebral cortex. FASEB J 2001;15:907–15.
2. Zhang D, Tai LK, Wong LL, Chiu LL, Sethi SK, Koay ES. Proteomic study reveals that proteins involved in metabolic and detoxification pathways are highly expressed in HER-2/neu-positive breast cancer. Mol Cell Proteomics 2005;4:1686–96.
3. Minami H, Kawada K, Murakami K, Sato T, Kojima Y, Ebi H, et al. Prospective study of positron emission tomography for evaluation of the activity of lapatinib, a dual inhibitor of the ErbB1 and ErbB2 tyrosine kinases, in patients with advanced tumors. Japanese J Clin Oncol 2007;37:44–8.
4. Dunnwald LK, Doot RK, Specht JM, Gralow JR, Ellis GK, Livingston RB, et al. PET tumor metabolism in locally advanced breast cancer patients undergoing neoadjuvant chemotherapy: value of static versus kinetic measures of fluorodeoxyglucose uptake. Clin Cancer Res 2011;17:2400–9.
5. Conklin MW, Provenzano PP, Eliceiri KW, Sullivan R, Keely PJ. Fluorescence lifetime imaging of endogenous fluorophores in histopathology sections reveals differences between normal and tumor epithelium in carcinoma *in situ* of the breast. Cell Biochem Biophys 2009;53:145–57.
6. Mujat C, Greiner C, Baldwin A, Levitt JM, Tian F, Stucenski LA, et al. Endogenous optical biomarkers of normal and human papillomavirus immortalized epithelial cells. Int J Cancer 2008;122:363–71.
7. Provenzano PP, Eliceiri KW, Keely PJ. Multiphoton microscopy and fluorescence lifetime imaging microscopy (FLIM) to monitor metastasis and the tumor microenvironment. Clin Exp Metastasis 2009;26:357–70.
8. Walsh A, Cook RS, Rexer B, Arteaga CL, Skala MC. Optical imaging of metabolism in HER2 overexpressing breast cancer cells. Biomed Opt Expr 2012;3:75–85.
9. Skala MC, Riching KM, Bird DK, Gendron-Fitzpatrick A, Eickhoff J, Eliceiri KW, et al. *In vivo* multiphoton fluorescence lifetime imaging of protein-bound and free nicotinamide adenine dinucleotide in normal and precancerous epithelia. J Biomed Opt 2007;12:024014.
10. Skala MC, Riching KM, Gendron-Fitzpatrick A, Eickhoff J, Eliceiri KW, White JG, et al. *In vivo* multiphoton microscopy of NADH and FAD redox states, fluorescence lifetimes, and cellular morphology in precancerous epithelia. Proc Natl Acad Sci U S A 2007;104:19494–9.
11. Walsh AJ, Cook RS, Manning HC, Hicks DJ, Lafontant A, Arteaga CL, et al. Optical metabolic imaging identifies glycolytic levels, subtypes,

and early-treatment response in breast cancer. Cancer Res 2013;73: 6164–74.

12. Chance B, Schoener B, Oshino R, Itshak F, Nakase Y. Oxidation-reduction ratio studies of mitochondria in freeze-trapped samples. NADH and flavoprotein fluorescence signals. J Biol Chem 1979;254: 4764–71.

13. Warburg O. On the origin of cancer cells. Science 1956;123:309–14.

14. Lakowicz J. Principles of fluorescence spectroscopy. New York: Plenum Publishers; 1999.

15. Campbell JJ, Davidenko N, Caffarel MM, Cameron RE, Watson CJ. A multifunctional 3D co-culture system for studies of mammary tissue morphogenesis and stem cell biology. PLoS ONE 2011;6:e25661.

16. Straussman R, Morikawa T, Shee K, Barzily-Rokni M, Qian ZR, Du J, et al. Tumour micro-environment elicits innate resistance to RAF inhibitors through HGF secretion. Nature 2012;487:500–4.

17. Chakrabarty A, Sanchez V, Kuba MG, Rinehart C, Arteaga CL. Feedback upregulation of HER3 (ErbB3) expression and activity attenuates antitumor effect of PI3K inhibitors. Proc Natl Acad Sci U S A 2012; 109:2718–23.

18. Miller TW, Forbes JT, Shah C, Wyatt SK, Manning HC, Olivares MG, et al. Inhibition of mammalian target of rapamycin is required for optimal antitumor effect of HER2 inhibitors against HER2-overexpressing cancer cells. Clin Cancer Res 2009;15:7266–76.

19. Xia W, Bacus S, Hegde P, Husain I, Strum J, Liu L, et al. A model of acquired autoresistance to a potent ErbB2 tyrosine kinase inhibitor and a therapeutic strategy to prevent its onset in breast cancer. Proc Natl Acad Sci U S A 2006;103:7795–800.

20. Walsh AJ, Poole KM, Duvall CL, Skala MC. Ex vivo optical metabolic measurements from cultured tissue reflect in vivo tissue status. J Biomed Opt 2012;17:116015.

21. Bird DK, Yan L, Vrotsos KM, Eliceiri KW, Vaughan EM, Keely PJ, et al. Metabolic mapping of MCF10A human breast cells via multiphoton fluorescence lifetime imaging of the coenzyme NADH. Cancer Res 2005;65:8766–73.

22. Wozniak MA, Keely PJ. Use of three-dimensional collagen gels to study mechanotransduction in T47D breast epithelial cells. Biol Proced Online 2005;7:144–61.

23. Nakashima N, Yoshihara K, Tanaka F, Yagi K. Picosecond fluorescence lifetime of the coenzyme of D-amino acid oxidase. J Biol Chem 1980;255:5261–3.

24. Lakowicz JR, Szmacinski H, Nowaczyk K, Johnson ML. Fluorescence Lifetime Imaging of Free and Protein-Bound Nadh. Proc Natl Acad Sci U S A 1992;89:1271–5.

25. Walsh AJ, Skala MC. An automated image processing routine for segmentation of cell cytoplasms in high-resolution autofluorescence images. SPIE Proc 2014;8948.

26. Akaike H. A new look at the statistical model identification. Automatic Control, IEEE Trans 1974;19:716–23.

27. Chakrabarty A, Bhola NE, Sutton C, Ghosh R, Kuba MG, Dave B, et al. Trastuzumab-resistant cells rely on a HER2-PI3K-FoxO-survivin axis and are sensitive to PI3K inhibitors. Cancer Res 2013;73:1190–200.

28. Shapiro GI, Rodon J, Bedell C, Kwak EL, Baselga J, Brana I, et al. Phase I safety, pharmacokinetic, and pharmacodynamic study of SAR245408 (XL147), an oral pan-class I PI3K inhibitor, in patients with advanced solid tumors. Clin Cancer Res 2014;20:233–45.

29. Ritter CA, Perez-Torres M, Rinehart C, Guix M, Dugger T, Engelman JA, et al. Human breast cancer cells selected for resistance to trastuzumab in vivo overexpress epidermal growth factor receptor and ErbB ligands and remain dependent on the ErbB receptor network. Clin Cancer Res 2007;13:4909–19.

30. Aurisicchio L, Marra E, Luberto L, Carlomosti F, De Vitis C, Noto A, et al. Novel anti-ErbB3 monoclonal antibodies show therapeutic efficacy in xenografted and spontaneous mouse tumors. J Cell Physiol 2012; 227:3381–8.

31. Blacker TS, Mann ZF, Gale JE, Ziegler M, Bain AJ, Szabadkai G, et al. Separating NADH and NADPH fluorescence in live cells and tissues using FLIM. Nat Commun 2014;5:3936.

32. Zhao Y, Butler EB, Tan M. Targeting cellular metabolism to improve cancer therapeutics. Cell Death & Dis 2013;4:e532.

33. Walsh AJ, Cook RS, Arteaga CL, Skala MC. Optical metabolic imaging of live tissue cultures. SPIE Proc 2013;8588.

34. Ostrander JH, McMahon CM, Lem S, Millon SR, Brown JQ, Seewaldt VL, et al. Optical redox ratio differentiates breast cancer cell lines based on estrogen receptor status. Cancer Res 2010;70: 4759–66.

35. Chang J, Powles TJ, Allred DC, Ashley SE, Makris A, Gregory RK, et al. Prediction of clinical outcome from primary tamoxifen by expression of biologic markers in breast cancer patients. Clin Cancer Res 2000;6: 616–21.

36. Arpino G, Green SJ, Allred DC, Lew D, Martino S, Osborne CK, et al. HER-2 amplification, HER-1 expression, and tamoxifen response in estrogen receptor-positive metastatic breast cancer: a southwest oncology group study. Clin Cancer Res 2004;10:5670–6.

37. Holmes FA, Walters RS, Theriault RL, Forman AD, Newton LK, Raber MN, et al. Phase II trial of taxol, an active drug in the treatment of metastatic breast cancer. J Nat Cancer Inst 1991;83: 1797–805.

38. Seidman AD, Tiersten A, Hudis C, Gollub M, Barrett S, Yao TJ, et al. Phase II trial of paclitaxel by 3-hour infusion as initial and salvage chemotherapy for metastatic breast cancer. J Clin Oncol 1995;13: 2575–81.

39. Velasco-Velazquez MA, Homsi N, De La Fuente M, Pestell RG. Breast cancer stem cells. Int J Biochem Cell Biol 2012;44:573–7.

40. Al-Hajj M, Wicha MS, Benito-Hernandez A, Morrison SJ, Clarke MF. Prospective identification of tumorigenic breast cancer cells. Proc Natl Acad Sci U S A 2003;100:3983–8.

41. Mohsin SK, Weiss HL, Gutierrez MC, Chamness GC, Schiff R, Digiovanna MP, et al. Neoadjuvant trastuzumab induces apoptosis in primary breast cancers. J Clin Oncol 2005;23:2460–8.

42. Dent R, Trudeau M, Pritchard KI, Hanna WM, Kahn HK, Sawka CA, et al. Triple-negative breast cancer: clinical features and patterns of recurrence. Clin Cancer Res 2007;13:4429–34.

43. Bauer KR, Brown M, Cress RD, Parise CA, Caggiano V. Descriptive analysis of estrogen receptor (ER)-negative, progesterone receptor (PR)-negative, and HER2-negative invasive breast cancer, the so-called triple-negative phenotype: a population-based study from the California cancer Registry. Cancer 2007;109:1721–8.

44. Aurisicchio L, Marra E, Roscilli G, Mancini R, Ciliberto G. The promise of anti-ErbB3 monoclonals as new cancer therapeutics. Oncotarget 2012;3:744–58.